THE GROWTH AND CHARACTERIZATION OF $Fe/TaO_x/Co$ MULTILAYERS FOR SPINTRONICS APPLICATIONS

A Thesis Submitted to
the Graduate School of Engineering and Sciences of
İzmir Institute of Technology
in Partial Fulfillment of the Requirements for the Degree of

MASTER OF SCIENCE

in Physics

by
Hüseyin TOKUÇ

July 2008
İZMİR

We approve the thesis of **Hüseyin TOKUÇ**

Assist. Prof. Dr. Süleyman TARI
Supervisor

Assoc. Prof. Dr. Hakan KÖÇKAR
Committee Member

Assoc. Prof. Dr. Salih OKUR
Committee Member

7 July 2008
Date

Prof. Dr. Durmuş Ali DEMİR
Head of Physics Department

Prof. Dr. Hasan BÖKE
Dean of the Graduate School of
Engineering and Science

ACKNOWLEDGEMENTS

I would like to thank to my advisor Assist. Prof. Dr. Süleyman TARI for his motivation, academic guidance and positive attitude during my master degree.

I would like to thank to Assoc. Prof. Dr. Salih OKUR for AFM and Dr. Gülnur Aygün for ellipsometry measurements. I acknowledge the Center of Material Research of İzmir Institute of Technology for X-Ray measurements and Department of Physics for providing Teaching Assistantship. I also thank to İzmir Institute of Technology for providing Research Assistantship and TUBITAK for funding the project ‘‘TBAG-105T109’’ during my thesis.

I am very thankful to Dr. İlbeyi Avcı, Berrin P. Algül and Barış Pekerten for their help during my study.

ABSTRACT

THE GROWTH AND CHARACTERIZATION OF Fe/TaO_x/Co MULTILAYERS FOR SPINTRONICS APPLICATIONS

In this thesis, the effect of Ta buffer layer and the thickness of the Ta_2O_5 barrier layer on the structural and magnetic properties of Fe/Ta_2O_5/Co multilayers have been studied. XRD and AFM techniques were used for structural investigations and VSM was used for investigation of magnetic properties. Refractive index of the barrier layer was determined by ellipsometry technique. In this study, magnetic tunnel junctions have also been fabricated by using photolithography technique and then electrical and magnetoresistance measurements were done.

The structural investigations showed that Ta under layer increases the crystalline quality of Fe layer and causes a change on magnetic parameters of Fe films. The AFM results showed that the range of the roughness for all layers is between 1.7 Å and 6.3 Å. When the thickness of the oxide layer was 4 nm, magnetic decoupling appears. Clear differences between the coercive fields of the ferromagnetic layers were observed in further increase of the barrier layer thickness. The effect of annealing on the Fe/TaO_x/Co multilayer was studied and it was found that only the coercivity of Fe film increases with increasing temperature up to the 250°C. Then, annealing at 400°C showed a sharp decrease in the coercivity of Fe film indicating an intermixing at the interface of Fe/TaO_x. Co minor loops showed that the magnetostatic coupling is large for thin barriers and decreases with increasing the barrier thickness. Electrical measurements showed that conduction occurs via tunneling electrons. However, no TMR ratio has been observed after magnetoresistance measurements.

ÖZET

SPİNTRONİK UYGULAMALARI İÇİN $Fe/TaO_x/Co$ ÇOKLU KATMANLARININ BÜYÜTÜLMESİ VE KARAKTERİZASYONU

Bu tezde, Ta alt tabakası ile Ta_2O_5 yalıtkan oksit tabakasının kalınlığının, $Fe/TaO_x/Co$ çoklu katmanlarının yapısal ve manyetik özellikleri üzerindeki etkileri incelenmiştir. Yapısal incelemelerde XRD ve AFM teknikleri, manyetik incelemelerde VSM ve oksit tabakasının kırılma indisinin ölçümünde de elipsometri teknikleri kullanılmıştır. Bu çalışmada ayrıca manyetik tünel eklemleri fotolitografi tekniğiyle üretilmiş ve sonra elektriksel ve manyetik-direnç ölçümleri yapılmıştır.

Yapısal incelemeler, Ta alt katmanının, Fe' in kristal özelliğini arttırdığını ve manyetik özelliklerinin değişmesine yolaçtığını göstermiştir. Yapılan AFM ölçümlerinde katmanların yüzey prüzlülüklerinin 1.7 Å ile 6.3 Å arasında değiştiği gözlenmiştir. Oksit tabakasının kalınlığı 4 nm olduğunda manyetik etkileşimsizlik gözlenmeye başlanmıştır. Oksit tabakasının kalınlığı arttırılmaya devam ettirildiğinde, ferromanyetik tabakaların coersivite alanları arasındaki fark açıkça gözlenmeye başlanmıştır. Tavlamanın çoklu katman üzerindeki etkisi araştırılmış ve $Fe/TaO_x/Co$ çoklu katmanının 250°C'ye kadar tavlanması, sadece Fe katmanının coersivite alanının arttığını göstermiştir. 400°C de tavlama, coercivite alanında keskin bir düşüşe neden olmuştur. Bu, Fe/TaO_x ara yüzeyinde bir oksijen karışımın olduğunu göstermiştir. Co minor histeresis eğrileri, ince oksit tabakası için manyetostatik etkileşimin büyük olduğunu ve oksit tabakasının kalınlığı arttıkça etkileşimin azaldığını göstermiştir. Elektriksel ölçümler iletimin tünelleme yapan elektronlar tarafında oluştuğunu göstermiştir. Ancak, manyetik ölçümlerin sonunda TMR oranı gözlenememiştir.

TABLE OF CONTENTS

LIST OF FIGURES

LIST OF TABLES

CHAPTER 1

INTRODUCTION

Magnetism is widely used in many research areas not only as a scientific branch but also due to its great application areas such as magnetic sensors and magnetic memories. The computer technology has been one of the most important areas of the application of magnetism, recently. In the 21st century, technological development requires denser, faster and smaller electronic devices as well as low power consumption in order to improve the functionalities. These requirements bring about using the spin property of the electrons in devices hence the name spintronics.

Spin is an intrinsic property of electrons and it is a purely quantum mechanical phenomena. Electrons have two different spin states, spin up and spin down. Using this property, it is possible to build devices in which the spin property of electrons is controlled. Spintronic devices have small operation size which can offer high storage information and faster operation speed because direction of spins can switch on the order of nano second. Moreover, spintronic devices such as MRAMs are non-volatile, that is when the power goes off, spins can keep their magnetization directions while in the conventional devices such as in DRAMs, capacitors lose their charges and memory assemblies refresh the all chips about 1000 times within a second by reading and re-writing the contents of the all chips. This situation requires a constant power supply, which is the reason why DRAMs lose their memory when power turns of. However, the MRAMs do not need the refreshing at any time and continuous power to keep the information. All these things offer that spintronics is an attractive research area for the storage information industry.

The effect of spin on the electrical resistance was firstly observed by Thomson (1856). He demonstrated that the electrical resistance of a ferromagnetic conductor depended on whether the current flowing through the conductor was perpendicular or parallel to the magnetization of the sample. When the current flows parallel to the magnetization vector of the sample, the strong scattering process occurs and high resistance is observed, $\rho_{\parallel}$. However, when the current and magnetization vector are perpendicular to each other, low scattering and low resistivity are observed, $\rho_{\perp}$. This

event has been called as anisotropic magnetoresistance effect (AMR). Although the AMR effect previously shows the relationship between spin and electrical resistance, the discovery of Giant Magnetoresistance (GMR) effect is considered as the birth of the spintronics. It was independently discovered for Fe/Cr/Fe trilayers (Binasch, et al. 1989) and for Fe/Cr multilayers (Baibich, et al. 1988). A typical GMR device consists of two ferromagnetic layers (FM) separated by a nonmagnetic (NM) spacer layer which behaves as a spin valve. The schematic of spin valve structure is shown in Figure 1.1.

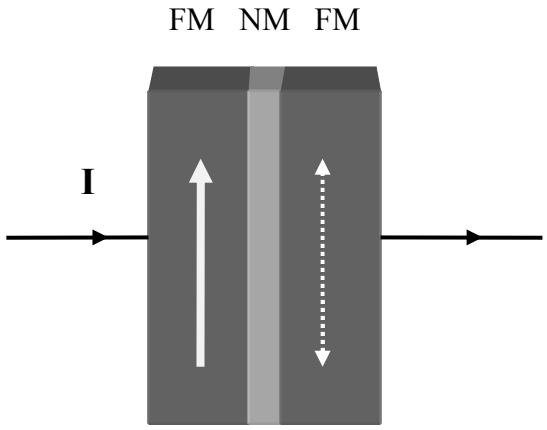

Figure 1.1. A typical GMR spin valve structure.

Operation principle of these devices depends on the relative alignment of magnetizations of the two FM layers one of which is pinned while the other one is free to rotate under external magnetic field. If the magnetization directions of the magnetic layers are antiparallel, the system shows high resistance. When they are aligned parallel, the resistance reaches its minimum value. The Figure 1.2 summarizes the operation principle of a simple GMR structure. In the Figure 1.2a, only the spin up electrons can pass without any scattering through the whole structure and spin down electrons scatter within the both layer then conduction is supplied by spin up electrons. However, in the Figure 1.2b, while only the spin down electrons scatter within the first layer, the spin up electrons do not scatter and for the second FM layer vice versa then system has a big resistance. The significant change of the resistance has been called as giant magnetoresistance and the value of the GMR is calculated by the following formula;

$$GMR = (\frac{R_{\uparrow\downarrow} - R_{\uparrow\uparrow}}{R_{\uparrow\uparrow}})x100$$

where $R_{\uparrow\downarrow}$ and $R_{\uparrow\uparrow}$ are the resistances of antiparallel and parallel alignment, respectively.

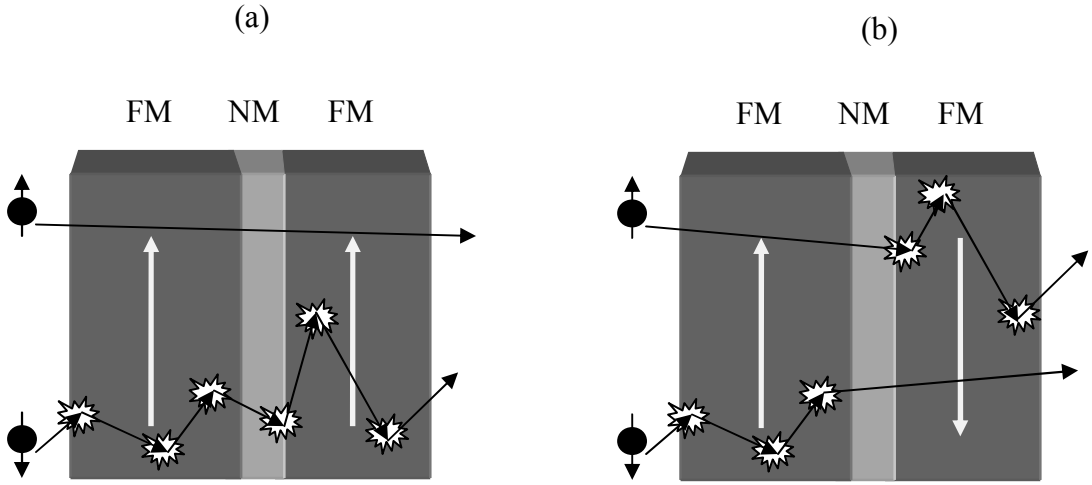

Figure 1.2. The figure of conduction in a GMR structure a) in parallel alignment and b) in antiparallel alignment.

The variation of the resistance from antiparallel to parallel configuration as a function of the applied magnetic field was observed for the Fe/Cr multilayers shown in Figure 1.3.

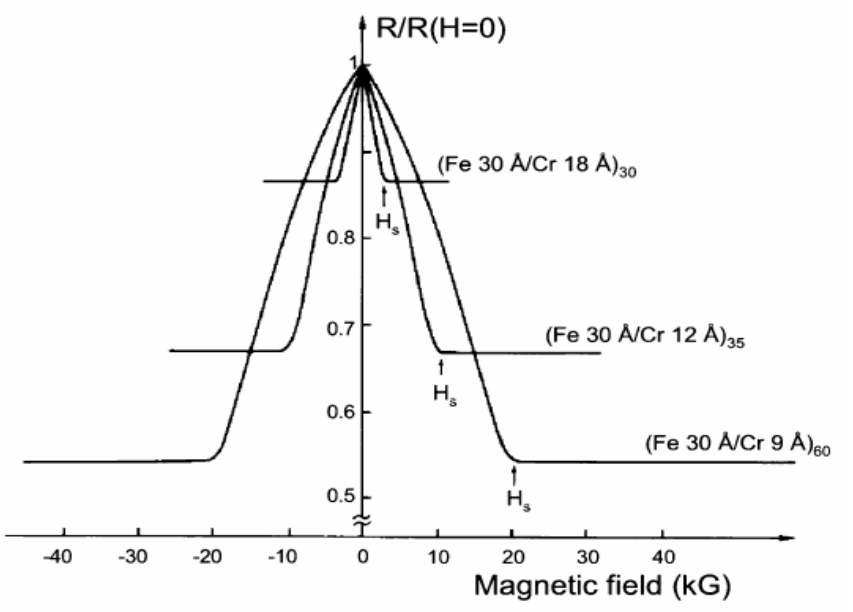

Figure 1.3. Magnetoresistance curve for Fe/Cr multilayers at low temperature.

The development of the spintronics has been going on with the discovery of tunneling magnetoresistance (TMR) effect. A simple TMR device consists of two FM layers which are separated by a NM insulating spacer layer. In the TMR devices, insulating layer should be very thin so that electrons can tunnel easily without any scattering which can cause changing the orientation of spins. The thickness of the insulating layers generally is about 1-2 nm (Hehn, et al. 2000). The operation principle of the TMR devices is the same with GMR devices and based on the relative alignment of the FM electrodes. However, the physical origin of TMR depends on the quantum mechanical tunneling phenomena of the wave function of electrons. The TMR ratio is defined as following formula;

$$TMR = (\frac{R_{\uparrow\downarrow} - R_{\uparrow\uparrow}}{R_{\uparrow\uparrow}})x100$$

Although the first experiment reported by Julliere (1975) at low temperature showed 14% TMR ratio for Co/oxidized Ge/Fe junctions, the significant change in the magnetoresistance at room temperature was observed for $CoFe/Al_2O_3/Co$ junctions with TMR ratio of 11% (Moodera, et al. 1995) and $Fe/Al_2O_3/Fe$ junctions with TMR ratio of 20% (Miyazaki and Tezuka 1995), where Al_2O_3 insulating layers were amorphous. Since that time scientists have been trying to improve TMR ratios of magnetic tunnel

junctions by using different ferromagnets (Fe, Co, Ni alloys) and some physical treatments. One of the most widely using methods is annealing process of the multilayers. Annealing of the multilayers under the suitable conditions almost doubles the TMR ratio (Sousa, et al. 1998). Furthermore, polycrystalline CoFe (Han, et al. 2000) and amorphous CoFeB (Wang, et al. 2004) electrodes show the TMR ratio of 50% and 70%, respectively. The other method in order to obtain high TMR ratio is to use of electrodes which have higher spin polarization at the Fermi level. This type of electrodes shows half metallic behavior such as CrO_2, Fe_3O_4, $La_{0.7}Sr_{0.3}MnO_3$, $La_{0.7}Ca_{0.3}MnO_3$, Sr_2FeMoO_6 types and Heusler alloys like NiMnSb or Co2MnSi (Alain and Daniel 2005). By using these types of electrodes, it has been possible to obtain very large TMR ratios at low temperatures. However, TMR ratio decreases and vanishes at near the room temperature for these electrodes (Bowen, et al. 2003). The last method in order to achieve high TMR ratios is using the crystalline MgO barrier instead of amorphous Al_2O_3 spacer layer. It is well known that crystalline structures have perfect ordered atoms in space and the number of structural defects is less than amorphous materials. Using a crystalline MgO barrier results in low scattering at the barrier layer with respect to amorphous layers and spins can keep their orientations. Thus, it is easy to obtain large TMR ratios with respect to the MTJs with amorphous Al_2O_3 barrier. The first experimental results about MgO barrier were reported for Fe/MgO/FeCo(001) multilayer and the TMR ratio was 60% at low temperature and it was very large when comparing to the same structure with amorphous barrier (13% at that temperature) (Bowen, et al. 2001). Then, dramatic increase in TMR ratio with MgO barrier has been observed in Fe/MgO/Fe single crystalline multilayer by using molecular beam epitaxy (MBE). The TMR ratio of 250% at low temperature and 180% at room temperature were observed (Yuasa, et al. 2004). Also 300% and 220% TMR ratios have been obtained for CoFe/MgO/CoFe polycrystalline multilayer after thermal annealing (Parkin, et al. 2004). Furthermore, Djayaprawira, et al. (2005) obtained 300% at low temperature and 230% at room temperature with CoFeB/MgO/CoFeB multilayer grown by magnetron sputtering, where CoFeB layers are amorphous but MgO layer is (001) textured. Finally, TMR ratio was achieved the value of %500 for CoFeB/MgO/CoFeB at room temperature (Lee, et al. 2007). Hence, single crystalline MgO has been widely used as a barrier layer in many magnetic tunnel junctions.

In this thesis, structural and magnetic properties of SiO_2/Ta/Fe/TaO_x/Co multilayer were studied. In order to determine the pinned and free layers, Fe, Ta/Fe,

$Ta/Fe/TaO_x$, Co and Ta/Co single and multilayers were analyzed by different characterization techniques. In chapter 2 the basics of magnetism, magnetic interactions, magnetic coupling phenomena and tunneling magnetoresistance were briefly mentioned. In chapter 3, the structural properties of the materials used in this study were explained. Experimental characterization techniques and growth kinetics were introduced in chapter 4. Results were presented and discussed in chapter 5. Finally, the summary is given in chapter 6.

CHAPHER 2

MAGNETISM

2.1. The Origin of Magnetism

Magnetism arises from the two kinds of motion of the electrons. The first one is orbital motion around the nucleus, which produces an orbital magnetic dipole moment and the other is rotation of the electrons around their own axis called as *spin*, which produces the spin magnetic dipole moment. Therefore, total magnetic dipole moment of an atom is the summation of these two types dipole moments. The Figure 2.1. shows the relationship between magnetic dipole moment and orbital motion of an electron, where μ and r represents the dipole moment and the radius of the orbital motion of electron, respectively, and υ is the velocity.

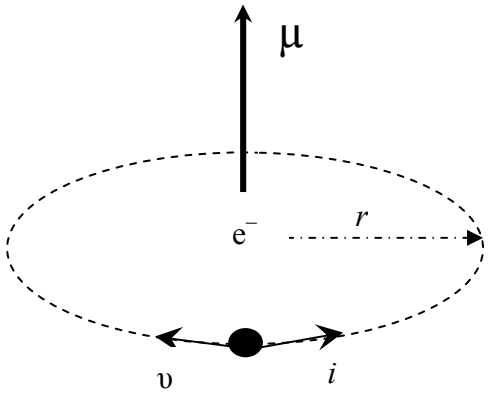

Figure.2.1. Relationship between magnetic dipole moment and orbital motion of an electron

The orbital magnetic dipole moment of this system is defined as $\boldsymbol{\mu} = i.\mathbf{a}$ and the period of the electron is defined as $\tau = \frac{2\pi r}{v}$. This orbital motion of the electron can be considered as a current *i*.

$$i = \frac{-e}{\tau} = \frac{-ev}{2\pi r}$$

Therefore, orbital magnetic dipole moment of an atom with a single electron is given by

$$\mu = \frac{-e\hbar}{2ml}$$

where $|\hbar\mathbf{l}| = m\upsilon r$ and $\hbar$ is the natural unit of angular momentum. Then, $\hbar$l becomes the vector of angular momentum and $|\mathbf{a}| = \pi r^2$. The value of constant terms in the equation (2.2) is $9{,}7 \times 10^{-24}$ JT^{-1}. This value is called as *Bohr magneton* (μ_B) and it is the natural unit of magnetic dipole moment. On the other hand, spin magnetic dipole moment of this system is defined as follows:

$$\mu = g_0 \mu_B s$$

Where $g_0 \approx 2$. we see that spin angular momentum of an electron creates magnetic dipole moment two times more than the orbital angular momentum. Then, the total magnetic dipole moment of an atom which has more than one electron is the summation of the total magnetic dipole moment of each electron and is given as

$$\mu = -\mu_B (L + 2S)$$

According to that information, an atom can be considered as a magnetic dipole moment. However, this property is only seen in the atoms which have unfilled shells because two electrons in the same orbital move in the opposite directions and their magnetic dipole moments cancel each other. This situation is explained by the Hund's rule. Each electron occupies the orbitals in minimum energy state, where firstly spin up electrons fill the orbitals. Then, if there are uncoupled electrons in the orbitals, only these uncoupled electrons can contribute to produce magnetic dipole moments. The rare earth and transition elements generally show this behavior (Hook and Hall 1990).

2.2. Types of Magnetism

Materials can be classified according to their response to an external magnetic field. Magnetization is proportional to the external magnetic filed and is given as

$$M = \chi H$$

where magnetization, M, is defined as magnetic dipole moment per unit volume ($M = \mu/V$) and χ is magnetic susceptibility. The magnetic susceptibility is a parameter that shows the type of magnetic material and the strength of that type of magnetic effect. If $\chi < 0$, diamagnetic behavior becomes dominant between the magnetic moments. However, if $\chi > 0$ and $\chi >> 0$, interaction between the magnetic moments is paramagnetic and ferromagnetic, respectively. The second identity used to classify the magnetic materials is the relative permeability ($\mu_r = 1+ \chi$).

2.2.1. Diamagnetism

Diamagnetism arises from the changing orbital motions of electrons under an external magnetic field. There is no any permanent magnetic moment in the diamagnetic materials. If a diamagnetic material is subjected to an external field, a force ($\boldsymbol{F}=q\boldsymbol{v}\times\boldsymbol{B}$) acts on electrons and the electrons are accelerated within the material and also their magnetic moments are modified. According to the Lenz law, direction of the accelerated electrons creates a magnetic field which is in the opposite direction with respect to the external field and the material gains a magnetization in that direction, which is the reason why this type materials are repulsed by external magnetic fields. Diamagnetic materials have negative susceptibility.

2.2.2. Paramagnetism

Paramagnetic materials have permanent magnetic dipole moments so they have a positive magnetic susceptibility in the presence of an external field. In contrast, in absence of the field magnetic moments align randomly. When an external field is applied to the paramagnets, their magnetic moments tend to align parallel to the

external field. However, interaction between the magnetic moments and external field is weak. Therefore, magnetic susceptibility of paramagnets is generally in the range of $0 < \chi \leq 1$.

2.2.3. Ferromagnetism

Ferromagnetism is a special form of the paramagnetism and it arises from the strong interaction between the permanent magnetic dipole moments. This strong interaction is valid when the temperature is below T_C, Curie temperature. Thermal agitation is dominated by exchange interaction at that temperature range and all magnetic moments align in one direction. Even if there is no external field, ferromagnets have a spontaneous magnetization. Ferromagnetic materials reach the saturation magnetization in the presence of an external field. When the external field is removed, magnetic moments can keep their orientations and material has a net magnetization called as *remanence magnetization*. Magnetic susceptibility of these type materials is much larger than the others and it increases exponentially with external fields ($\chi >> 1$).

Fe, Co and Ni are the most famous FM elements. They show paramagnetic behavior above the T_C. Table 2.1 shows the Curie temperatures of some ferromagnets.

Table 2.1. Curie temperature of some ferromagnetic materials

Material	T_C (°K)
Fe	1043
Co	1394
Ni	631
Gd	317
Fe_2O_3	893

Magnetic parameters of FM materials such as saturation magnetization, coercive field, remanence magnetization as well as domain behaviors are obtained by using the hysteresis loops. A typical hysteresis loop is like in Figure 2.2 (magnetization versus applied field).

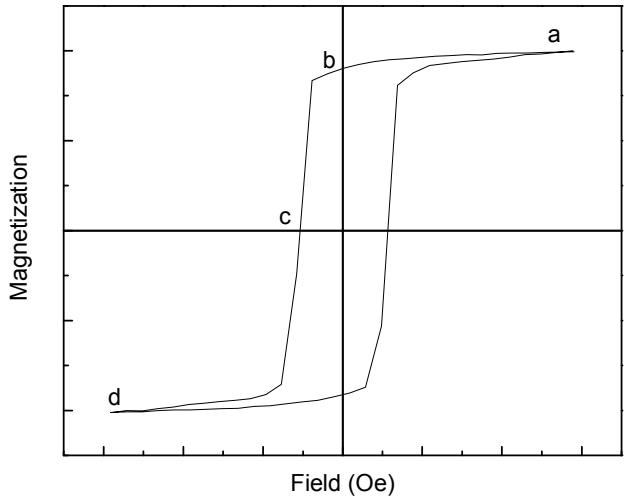

Figure.2.2. The hysteresis loop of a ferromagnet. a, b and c represent the saturation magnetization (M_s), remanence magnetization (M_r) and coercive field (H_c), respectively.

When all the magnetic moments align along the applied field in a ferromagnet, the material reaches the saturation point (point a). If the external field is applied in the opposite direction, the loop is not reversible. When the external field reaches to the zero, magnetic material has still a net magnetization called as remanence magnetization (point b). Next, when the net magnetization of the magnetic material becomes zero, the external field reaches the point *c* called as coercive field (H_c).

2.3. Exchange Interaction

Exchange interaction is an electrostatic interaction and it is responsible for the ferromagnetic behavior. Wavefunction of the electrons is antisymmetric and they can not be found at the same spin state and in the same place on space. Therefore, antisymmetric nature of the wavefunction forces to keep the electrons apart from each other in parallel alignment and reduces the Coulomb repulsion energy which is smaller for parallel alignment than antiparallel alignment. This situation is called as *exchange interaction*. The exchange interaction energy between atoms is defined as $E_{ex}=-2J_{ex}\boldsymbol{S_i}\boldsymbol{S_j}$, where $\hbar\boldsymbol{S_i}$ and $\hbar\boldsymbol{S_j}$ are the spin angular momenta of the i^{th} and j^{th} atoms respectively, and J_{ex} is the exchange integral. Because of this interaction, neighboring magnetic ions align

parallel (ferromagnetism) or antiparallel (antiferromagnetism) to each other. This interaction can be explained into the three groups.

2.3.1. Direct Exchange

Direct exchange is a strong interaction between the magnetic moments in small interatomic distances. However, this interaction decreases rapidly when the magnetic moments separate from each other. If two atoms are close to each other, their valance electrons spend most of their time in between the nuclei. Therefore, spin states of the electrons must be antiparallel because of the antisymmetric wavefunction and also the Pauli's exclusion principle. The antiparallel alignment gives rise to negative exchange.

Figure 2.3. Antiparallel alignment for small interatomic distances

If the interatomic distance is large between the atoms, the electron-electron interaction is minimum and electrons favor the parallel alignment to reduce the Coulomb energy and also J_{ex} becomes positive.

Figure 2.4. Parallel alignment for large interatomic distances

The interatomic exchange integral (J_{ex}) can have positive or negative values. The sign is determined by the balance between the Coulomb and kinetic energies. Figure 2.5 (the Bethe-Slater curve) shows the variation of J_{ex} with respect to the interatomic distance. For small distances J_{ex} is negative and represents the antiparallel alignment (antiferromagnet) and for large distances J_{ex} is positive (ferromagnetism). In spin valve structures, direct exchange may occur between magnetic electrodes through the spacer via pinholes.

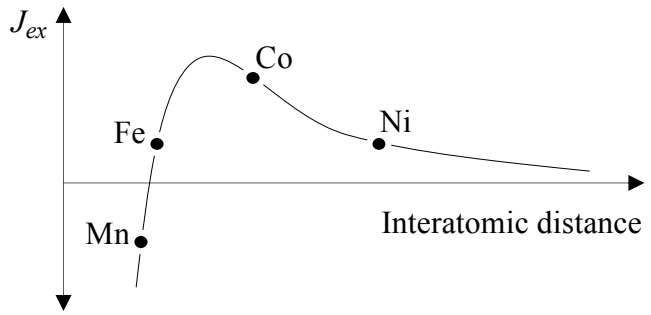

Figure.2.5. The Bethe-Slater curve

2.3.2. Indirect Exchange

This type of interaction causes the coupling of atomic magnetic dipole moments at large distances and is known as RKKY (Ruderman-Kittel-Kasuya-Yosida) interaction. It is generally seen in metals and occurs via the conduction electrons. A magnetic ion polarizes the conduction electrons around it via the exchange interaction and these polarized conduction electrons are sensed by another magnetic ion at a certain distance. The form of coupling is $-2J_{ex}\mathbf{S}_i\mathbf{S}_j$, where J_{ex} oscillates from positive sign to negative and its magnitude damps with the increasing distance between magnetic ions. Depending of the sign of J_{ex}, interaction can be ferromagnetic or antiferromagnetic. The variation of exchange integral versus interatomic distance is shown in the Figure 2.6. This type of interaction may occur in spin valve structures when the thickness of the spacer layer is bigger than a few nanometer.

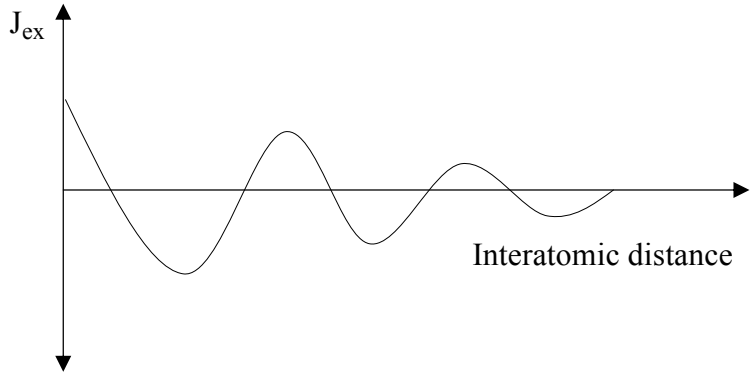

Figure 2.6. Indirect exchange versus the interatomic distance

2.3.3. Superexchange

This type of interaction is generally seen between the transition metal ions at large distances and mediated by a *p* ion which is in the ground state. The p_x orbital of the *p* ion has two electrons which have opposite spins in the ground state and this ion shares each of its electrons with the adjacent 3d orbitals. The shared electrons prevent their spin orientations. The resulting spin configurations within the 3d shells determine the coupling mechanism.

To better understand this event, let's consider the two transition ions, $3d^6$, and a double ionized oxygen molecule, O^{-2}, as shown in the figure. Z. The p_x orbital of the oxygen molecule is in the ground state (two opposite spins) and shares the electrons with the transition ions. The transition ions have unfilled 3d shells and according to the minimum energy configuration, the first 5 electrons must be in the same spin orientation and the 6^{th} electron must be in the opposite. Therefore, if the first ion forms a bond with the spin up electron, the first 5 electrons have spin down orientation. Then, the second transition ion forms a bond with the spin down electron of the p_x orbital and the configuration of the first 5 electrons becomes spin up. Thus, the two transition ions have an antiparallel orientation with respect to the each other.

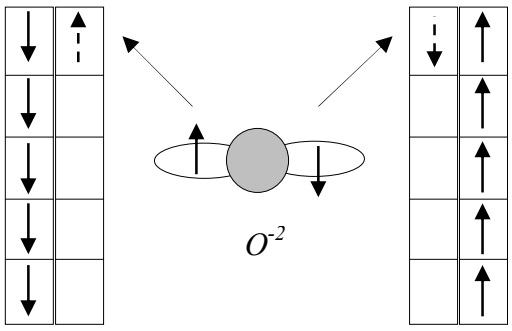

Figure 2.7. Two transition ions couples each other antiferromagnetically via an oxygen ion

2.4. Magnetic Domains

Ferromagnetic materials consist of small regions called *magnetic domains.* All magnetic moments within one domain align in the same direction. Magnetic domains are isolated from each other by *domain walls*. They are small transition regions between the two domains and play an important role for characterizing the magnetic properties of ferromagnetic materials.

Magnetic domains occur to minimize the magnetostatic energy. This minimum energy state is only achieved when the energy contributions of stray field and domain wall become minimum (Hook and Hall 1995). Then, domain size reaches to an ideal value. If the size of a magnetic particle is larger than the ideal value, energy contribution of the stray field is dominant with respect to the formation of new domain wall energy. Then, new domain walls are formed by division into two domains to reduce the energy of stray field (Figure 2.8). However, formation of the new domain walls increases the total energy of the system. Therefore, the division into domains only continues as long as the reduction in magnetostatic energy is greater than the energy required to form the domain wall (Kumar 2004). If the size of magnetic particles is smaller than the ideal value, the wall energy becomes larger than the stray field energy and division into the domains stops. Particles those are below this critical sizes called as *single domain particles*. Table 2.2. illustrates the critical single domain sizes some magnetic materials.

Table 2.2. Critical sizes of some spherical magnetic materials with no shape anisotropy.

Material	D_{crit}(nm)
Fe	70
Co	14
Ni	55
Fe_3O_4	128
γ-Fe_2O_3	166

Critical sizes arise from the competition between exchange coupling and magnetostatic energy and it depends on the geometry, anisotropy and saturation magnetization of the particles. If the exchange length is enough to dominate the magnetostatic field, single domain can form easily because of the strong exchange interaction.

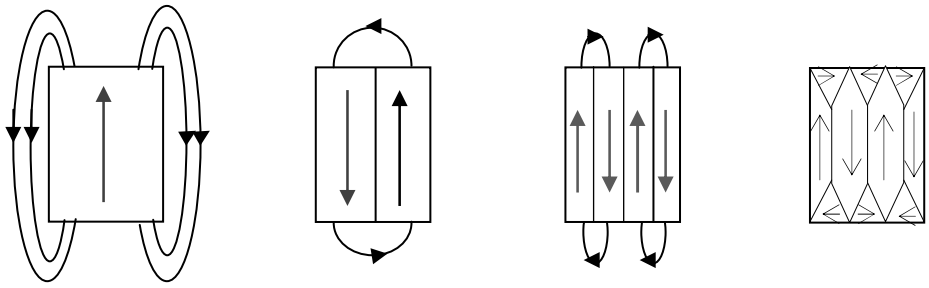

Figure 2.8. Formation of new domains causes decreasing of the energy within the stray field

As it is defined above, all magnetic moments align at a certain direction within one domain in the absence of an external field. This preferred direction called as *easy axes* and its orientation is in the different directions for the different domains.

2.5. Magnetic Anisotropy

Magnetic anisotropy is one of the most significant factors in order to characterize the magnetic materials and it may strongly affect the shape of the magnetic hysteresis loop. The simple explanation of anisotropy is that magnetic properties of a magnetic sample depend on the direction they are measured. The most important types of magnetic anisotropies are magnetocrystalline, shape and exchange anisotropies.

2.5.1. Magnetocrystalline anisotropy

Magnetocrystalline anisotropy can be thought as a force to keep the orientation of magnetic moments in a certain direction. Magnetic moments generally prefer to align along one direction of a crystalline cubic structure as an easy axis. Easy axis results from the spin-orbit coupling between the spin and orbital motion of an electron and less field require magnetizing the sample at that direction. The orbital motion of an electron is strongly affected by the lattice point (crystal field). Then, this effect is seen on the spin angular momentum of the electrons because of the spin-orbit coupling. Therefore, there is a correlation between the crystal field, orbital angular momentum and spin angular momentum of an electron. When an external force tries to rotate the spin of one

electron, the orbit of that electron also tends to rotate. However, orbital motion fixed by crystal field blocks the reorientation of spin axis. Thus, magnetic dipole moment of the electron aligns along a preferred direction under these interactions. The energy required to overcome the spin-orbit coupling and rotate the spins away from the easy axes is called as anisotropy energy. Quantitative measurement of magnetocrystalline anisotropy field, H_a, can be determined by saturating the sample in the hard axes in which the field required to magnetize the sample to saturation is largest. Figure 2.9. shows the relative crystallographic directions for easy and hard axis of hcp cobalt structure and their magnetization curves.

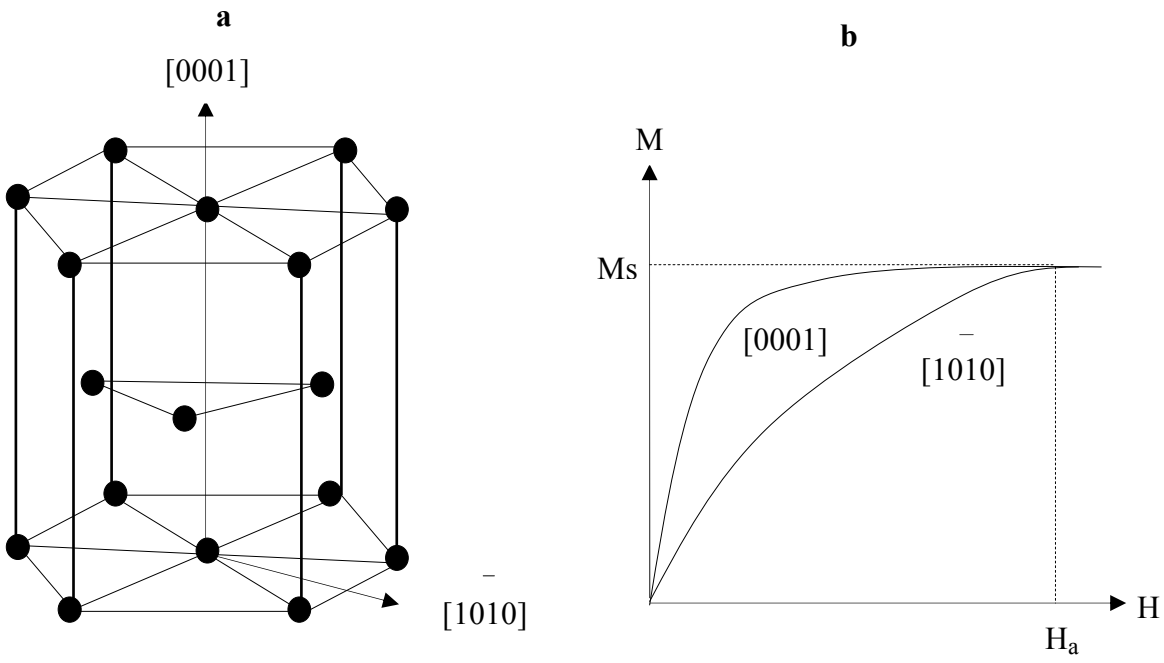

Figure 2.9. a) Crystallographic hcp structure of cobalt and b) easy and hard direction magnetization curves

The *c* axis is defined as magnetocrystalline easy axis and any direction in the basal plane is defined as hard axis. The stored energy difference between the easy and hard axis is the magnetocrystalline anisotropy energy (E_a) and it is expressed as following formula;

$$E_a = K_0 + K_1 Sin^2\theta + K_2 Sin^4\theta + \ldots$$

where K_i *is the* energy density and θ is the angle between magnetization vector and easy axis. However, for symmetric cubic crystals, the anisotropy energy is calculated by using the direction cosines of the magnetization with respect to the crystal axes and is defined as

$$E_a = K_0 + K_1(\alpha_1^2\alpha_2^2 + \alpha_2^2\alpha_3^2 + \alpha_1^2\alpha_3^2) + \cdots$$

where $\alpha_i = \text{Cos}\,\theta_i$ is the angle between magnetization and i^{th} axis.

2.5.2 Shape Anisotropy

The shape anisotropy depends on the dimensions of magnetic materials and results from the demagnetizing factor. A magnetized sample produces magnetic poles on the surface and these poles create another magnetic source called as demagnetizing field (H_d). The demagnetizing field lies in the opposite direction of the field forming it. Then, the net field (H_i) inside the specimen becomes

$$H_i = H - H_d$$

where H_d is the demagnetizing field. The demagnetizing field is proportional to the magnetization and the proportionality constant is described as demagnetizing factor, $H_d = N_dM$. N_d depends on the geometry of the specimen. In order to understand the effect of demagnetizing field on the shape anisotropy, a needle type specimen can be useful. When an external field magnetizes the specimen in Figure 2.10, the demagnetizing field along the long axis is less than along the short axis. Then, the long axis behaves as an easy axis. However, this situation can not be seen in the spherical samples because they have no shape anisotropy.

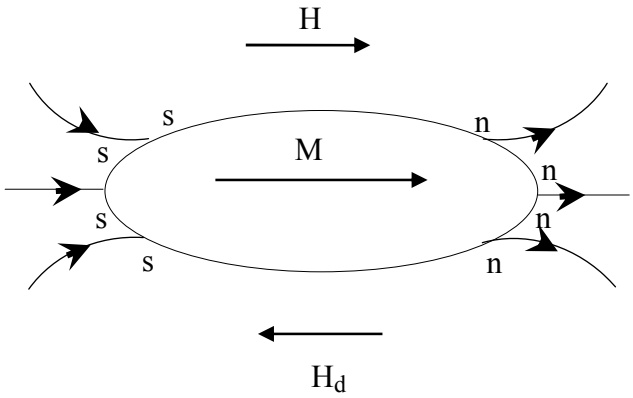

Figure 2.10. The demagnetizing field produced by surface pole distribution

2.5.3 Exchange Anisotropy

Exchange anisotropy (exchange bias) is one of the most important types of anisotropy used in many technological applications such as magnetoresistive devices. It was discovered by Meiklejohn and Bean (1957) and it results from an interaction between ferromagnetic and antiferromagnetic layers. When a FM/AFM system is cooled down below the Neel temperature, which is a specific temperature for transition between antiferromagnetic and paramagnetic phases for antiferromagnets, under an external field the spins of the second layer become antiferromagnetically ordered and they exert a torque on the spins of the FM layer to keep them their original direction. It is difficult to rotate the direction of an antiferromagnet with respect to a ferromagnet. Because of the torque, ferromagnetic layer can not be rotated easily with the external field in the FM/AFM system but it is easy to rotate if the external field is in the original magnetization direction of the ferromagnetic layer. These two effects cause a shift in the hysteresis loop on the field axis. Figure 2.11 shows the anisotropy process schematically.

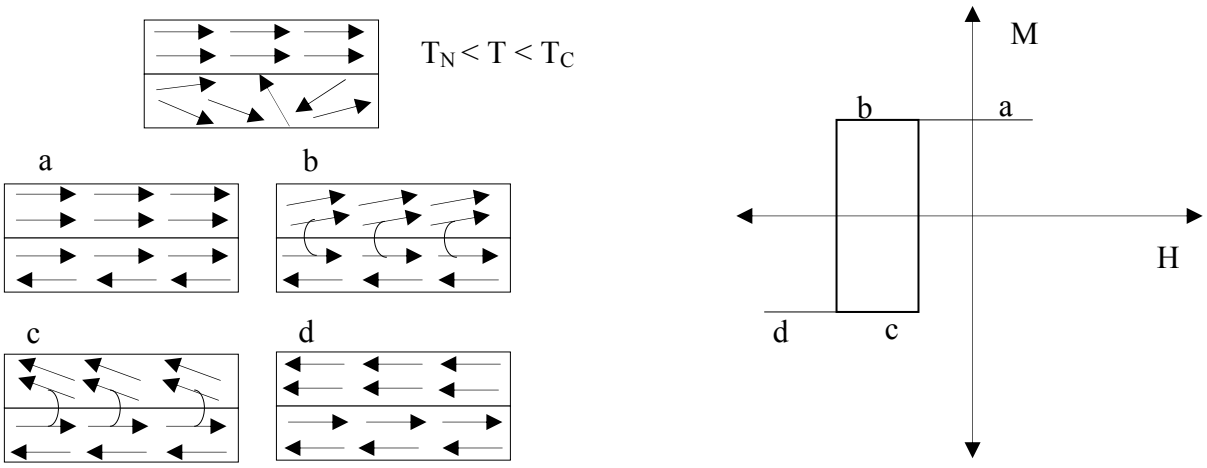

Figure 2.11. Schematic representation of spins dynamic in FM/AFM exchange biased system

2.6. Tunneling Magnetoresistance

The physical origin of the operation of MTJ structures is based on spin dependent scattering process of the electrons within the ferromagnetic layers. It is well known that ferromagnetic materials such as Fe, Co and Ni have different density of states (DOS) for the spin up (majority electrons) and spin down electrons (minority electrons) at the Fermi level because of the exchange interaction between the electrons (Figure 2.12b). These electrons called as *spin polarized electrons*. In contrast, number of the spin up and down electrons has the same value for normal metals at the Fermi level (Figure 2.12a).

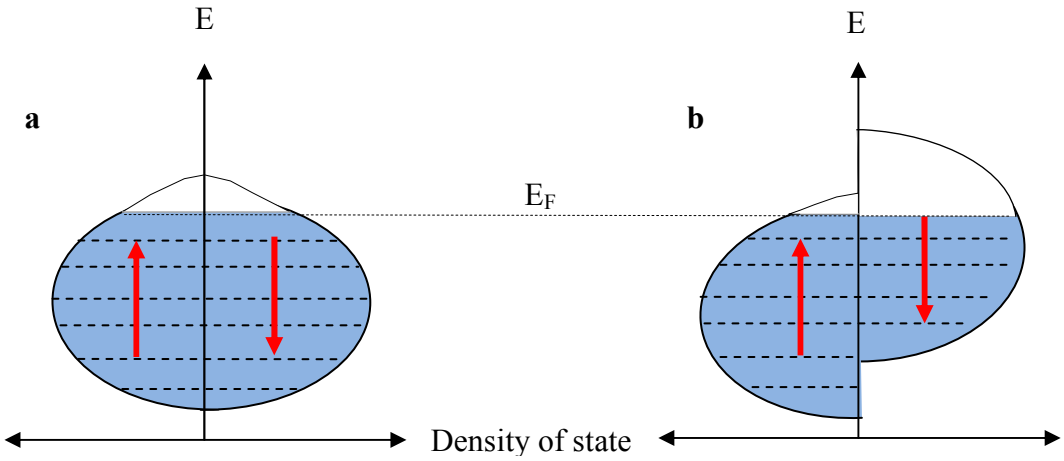

Figure 2.12. Schematic representation of DOS a) for a normal metal and b) for a ferromagnetic metal (arrows show majority and minority spin states)

The different DOSs lead to specific transport behavior of the majority and minority spin electrons in a FM material (Mott 1936). If the two FM layers have different DOS at the Fermi level, the polarized electrons which are located at the high energy levels in one electrode starts to move to the other electrode which has lower energy states at the Fermi level in order to achieve minimum energy configuration. When the electrons reach to the other FM layer, spin dependent scattering may occur due to the polarization of DOS of that layer. The Figure 2.13 shows the spin dependent scattering in a FM. The same things can be thought for GMR structures. During the same process there is no any spin dependent scattering within the nonmagnetic spacer layer because there are a lot of empty energy states for spin up and down electrons. Furthermore, number of these states is equal so spacer layer does not act as a restrictive layer on the electron motion.

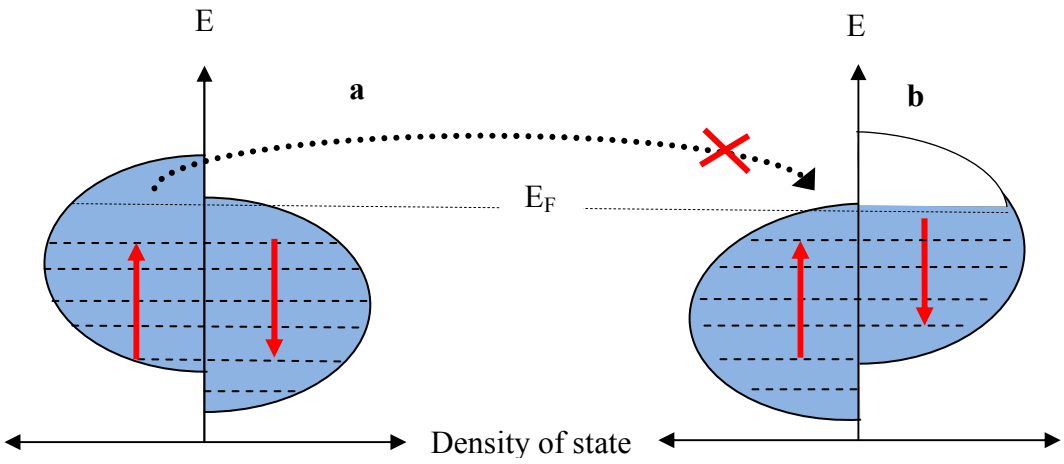

Figure 2.13. The DOS of two antiparallel ferromagnets and spin dependent scattering

The transport mechanism of the electrons within the insulating layer is the tunneling phenomenon which is a quantum mechanical effect. Electrons have both particle and wave like properties. Tunneling is a wave like effect of electrons. When electrons come across an energy barrier, their wave functions do not end abruptly and can pass through the barrier although the energies of electrons are less than the energy barrier. Then, same electrons can appear on the other side of the barrier. However, this effect can not be classically observed. The Figure 2.14 shows the tunneling effect.

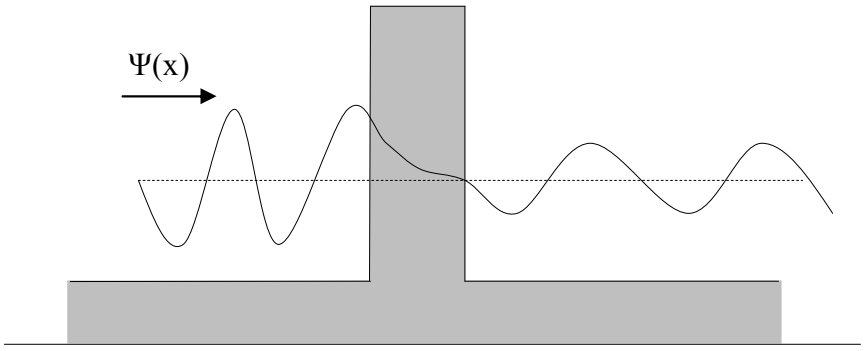

Figure 2.14. Wave function exponentially decays within the energy barrier

In magnetic tunnel junctions, electrons tunnel from one electrode to the other electrode and there exists a tunnel current if the electrodes have different Fermi energy. In order to create a potential difference between the electrodes a bias voltage (eV) is

applied. Typical band diagram of metal/insulator/metal junction under a bias voltage is shown in Figure 2.15.

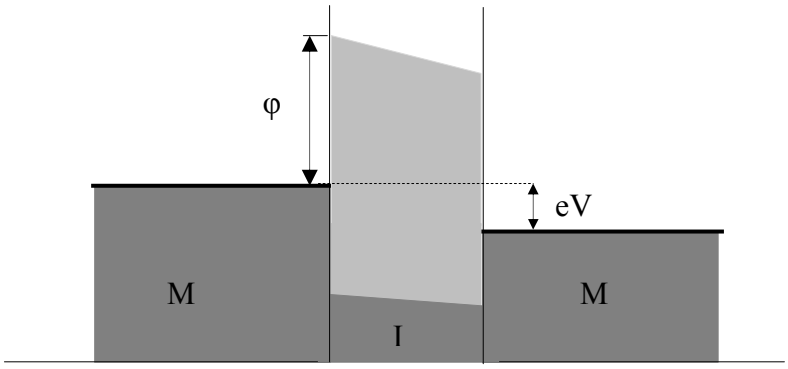

Figure 2.15. Band diagram of metal/insulator/metal structure

The existing tunneling current from the left electrode to the right electrode depends on the density of states of the first electrode, ρ (E), and the second electrode, ρ (E+eV), in the same energy, square of matrix element $|M|^2$, which represents the probability of transmission through the barrier, occupation probabilities that states in the left electrode, f (E), and probability that the states in the right electrode are empty. The resulting tunneling current is given by

$$I_{l\to r}(V) = \int_{-\infty}^{+\infty} \rho_l(E).\rho_r(E+eV).|M|^2.f(E).[1-f(E+eV)]dE$$

and the total current can be described as $I_{l\to r}$ - $I_{r\to l}$. For this type junctions, Simmons defined a tunneling current density and expressed it as following formula

$$J(V) = \frac{j_0}{d^2}\left(\varphi - \frac{eV}{2}\right)exp\left[-Ad\sqrt{\varphi - \frac{eV}{2}}\right] - \frac{j_0}{d^2}\left(\varphi + \frac{eV}{2}\right)exp\left[-Ad\sqrt{\varphi + \frac{eV}{2}}\right]$$

where J(V) represents the tunneling current density, A and j_0 are the constant of $4\pi\sqrt{2m_e^*/h}$ and $e/2\pi h$, respectively, φ is the average barrier height, d is the barrier thickness, V is the applied bias voltage and m_e^* is the effective mass of the electron (Simmons 1963). This term shows a linear behavior in small voltages. However, it has a non-linear characteristic for larger voltages, which is the evidence that current occurs

by tunneling electrons in M/I/M structures. It can also be seen that tunneling current shows exponential dependence on the thickness and average barrier height. This expression can be used only for symmetric structures, the left and right electrodes are identical, for asymmetric structures Brinkman's calculation is used (Brinkman, et al. 1970).

In the case of the tunneling magnetoresistance, TMR ratio strongly depends on the spin polarized electrons and conduction must be supplied by the spin up and down electrons.

$$TMR = \frac{R_{\uparrow\downarrow} - R_{\uparrow\uparrow}}{R_{\uparrow\uparrow}} = \frac{2P_1P_2}{1 - P_1P_2}$$

where P_1 and P_2 are the polarization of first and second ferromagnetic electrodes, respectively. Polarization of a ferromagnet defined as

$$P = \frac{D_{\uparrow}(\varepsilon_F) - D_{\downarrow}(\varepsilon_F)}{D_{\uparrow}(\varepsilon_F) + D_{\downarrow}(\varepsilon_F)}$$

where $D_{\uparrow}(\varepsilon_F)$ and $D_{\downarrow}(\varepsilon_F)$ are the density of states of ferromagnetic layers at the Fermi level.

2.7. Coupling Mechanism in TMR Spin Valve Structures

In the spin valve structures, low field and low power are desired for operational purposes. However, it is not always easy to obtain these desirable parameters because of coupling mechanisms between the FM layers. These coupling fields strongly affect the independent switching of the magnetic layers.

There are mainly three types of coupling field in the spin dependent tunnel junctions. The indirect exchange coupling, the fringe field coupling and magnetostatic interface coupling. As discussed above, indirect exchange coupling results from the polarization of conduction electrons within the nonmagnetic layer. However, the effect of this type coupling is small in the TMR devices at low applied voltages because there are less conduction electrons to tunnel through to the barrier. The fringe field becomes important when the lateral size is small and the thickness of the ferromagnetic layers is large. It is much less than 1 Oe if the lateral size and thickness of a sample are in the

order of mm and 10 nm, respectively (Wang, et al. 2000). Therefore, only the effect of interface coupling field is responsible for the coupling mechanism between the FM layers in these large samples. The interface coupling includes pinholes coupling, Neel wall coupling and Neel coupling (orange-peel coupling).

2.7.1. Pinhole Coupling

The pinhole coupling occurs when the thickness of the barrier layer is very thin. The direct interaction is responsible for this type coupling. When the barrier thickness is very thin, small pinholes can exist during the deposition process of the barrier and they act as a conduction bridge. Then, two FM layers contact with each other via the conduction bridges through the nonmagnetic (NM) layer. If the NM layer is an insulator instead of a conducting metal, pinhole coupling can be easily determined from I-V characteristic. Pinholes cause a shortcut between the magnetic layers and linear conduction is seen rather than tunneling. Figure 2.16 represents the pinhole coupling.

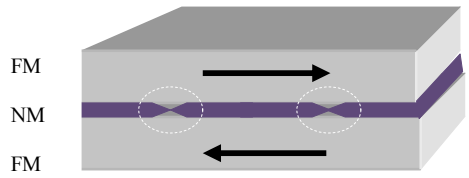

Figure 2.16. Small pinholes inside the encircled regions causes the coupling through the very thin nonmagnetic layer.

2.7.2. Neel Coupling (Orange-peel Coupling)

The Neel coupling is a roughness dependent coupling and tends to be parallel alignment of the magnetic layers. During the deposition process of the fixed magnetic layer, a sinusoidal surface roughness can exist and magnetic poles occur on the bumps. These poles create magnetic stray fields and they are sensed by the second magnetic layer. Then, ferromagnetic coupling exist between the two magnetic layers. If the magnetizations of two layers are parallel, magnetostatic charges of opposite signs appear symmetrically. In contrast, if the magnetizations are antiparallel, charges of the

same signs are facing each other leading to an increase in energy. This causes an effective FM coupling which has low energy between the two magnetic layers. As the barrier thickness increases, coupling field strength decreases exponentially. The field strength is given by the following equation,

$$H_N = \frac{\pi^2}{\sqrt{2}}\left(\frac{h^2}{\lambda t_F}\right) M_s \exp\left(-2\pi\sqrt{2}t_s/\lambda\right)$$

where h and λ are the amplitude and wavelength of the roughness, t_F and t_S are the thickness of the free and barrier layer, M_s is the saturation magnetization of the free layer. Figure 2.17 represents the roughness induced stray fields between two FM layers separated by a NM layer.

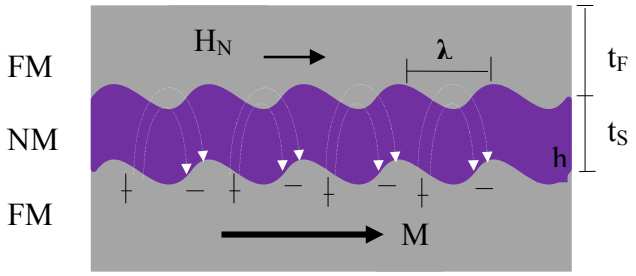

Figure 2.17. The roughness induced Neel coupling

2.5.3. Neel Wall Coupling

This type of coupling arises from the domain wall stray fields. Spin orientation changes from 0° to 180° within a Neel type domain wall and magnetic pole density occurs at the domain boundaries. This pole density creates magnetic stray fields which can exert a force on the adjacent magnetic layer. Domain wall motion of a single layer effects the other neighboring domain wall and the two layer switches together. In a multilayer structure, domain wall coupling makes the Hc of the whole layer smaller than that of a single layer. For spin valve structures, the effect of this coupling can be eliminated by creating the two different coercivities for magnetic layers. The Figure 2.18 shows the induced stray field of a Neel type domain wall and coupling mechanism.

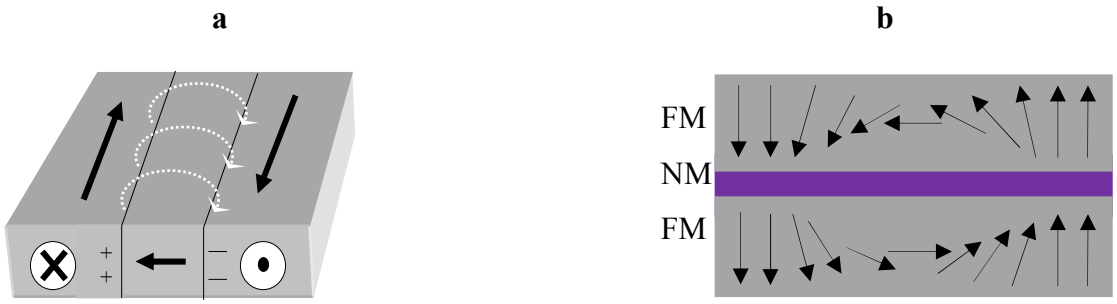

Figure 2.18. a) Induced stray field on domain boundaries and b)Neel wall coupling between the two magnetic layers. The spin orientations inside the walls tend to be opposite in order to reduce dipole-dipole interaction energy for each domains (Wang, et al. 2000)

CHAPTER 3

MATERIAL PROPERTIES

In this chapter, structural and magnetic properties of Fe, Co, Ta, and Ta_2O_5 will be discussed. These materials have been used for producing the MTJ structures in this thesis.

3.1. Iron (Fe)

Iron is a transition metal in group VIII with body-centered cubic crystalline structure, Figure 3.1. At ambient temperature the lattice constant is 2.86 Å and the electrical resistivity is 9.6 μΩ.cm.

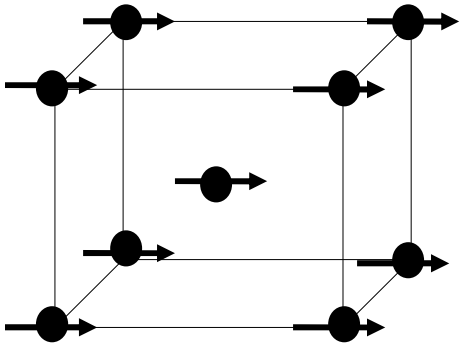

Figure 3.1. BCC crystalline structure of bulk iron and arrangements of atomic dipole moments due to the ferromagnetic coupling

Iron is the most important ferromagnetic material among the 3d transition metals. Its atomic number is 26 and electronic configuration is ended by $3d^6$. This means that there are 4 empty states within the d shell and according to the Hund's rule four spin up electrons remain unpaired. Ferromagnetism of iron only results from the these unpaired electrons in the atomic level. As it is discussed in chapter 1, there is an exchange splitting in the DOSs of FM materials in order to reach the minimum energy configuration. This situation results in a spin polarization at the Fermi level and a net

magnetic dipole moment is created. For iron the net magnetic moment is 2.2 μ_B and magnetization value (bulk) is 1714 emu/cm^3. Its coercive field is around 20 Gauss and the Curie temperature of iron is 1043 K.

3.2. Cobalt (Co)

Cobalt is also one of the 3d transition metals in group IX. It has two different crystalline orders in the nature; face-centered cubic (fcc) and hexagonal closed packed (hcp). At ambient temperature crystalline order is in the hcp structure but when the temperature increases up to the 415 °C, stable fcc structure exists (Kumar and Gupta 2007). Figures 2.4a. and 3.2. show the hcp and fcc crystalline structures, respectively. Electrical resistivity of cobalt is 6.24 μΩ.cm. at room temperature. The lattice parameters are a=b= 2.507 Å, c= 4.069 Å for hcp structure and a= 3.544 Å for fcc structure.

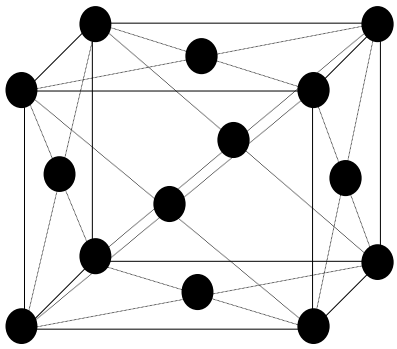

Figure 3.2. FCC cubic structure of cobalt

Cobalt's atomic number is 27 and electronic configuration is ended by $3d^7\ 4s^2$. It has three unpaired electrons in the d shell, which causes the ferromagnetic behavior. Magnetization value of bulk cobalt is 1422 emu/cm^3 and the Curie temperature is 1130 K. The net magnetic moment is 1.7 μ_B. Many magnetic sensors and memory devices include cobalt and cobalt based alloys because of its high spin polarization at the Fermi level (Hardley, et al. 2002). Therefore, magnetic properties make it very attractive for technological applications such as spin valve devices.

3.3. Tantalum (Ta) and Tantalum Oxide (TaO_x)

Tantalum is another transition element and found in V group in the periodic table. Its electronic configuration is ended by $5d^3$ $6s^2$. In the nature, there are two different crystalline structure of Ta: Body-centered cubic and tetragonal β structures as seen in Figure 3.3 (Liu, et al. 2001). However, formation of these structures depends on the deposition parameters and they have different mechanical and electrical properties. The lattice parameters of β-tantalum are a=b=10.19 Å, c=5.31 Å and for bcc structure a=b=c=3.30 Å. The bcc tantalum is used in many applications as a coating material for its toughness, ductility, low electrical resistivity (15-60 μΩ.cm) and corrosion resistance. Unlike bcc structure, β-phase tantalum is less desirable in many applications except for thin film resistor due to its high resistivity of 170-210 μΩ.cm (Jiang, et al. 2005).

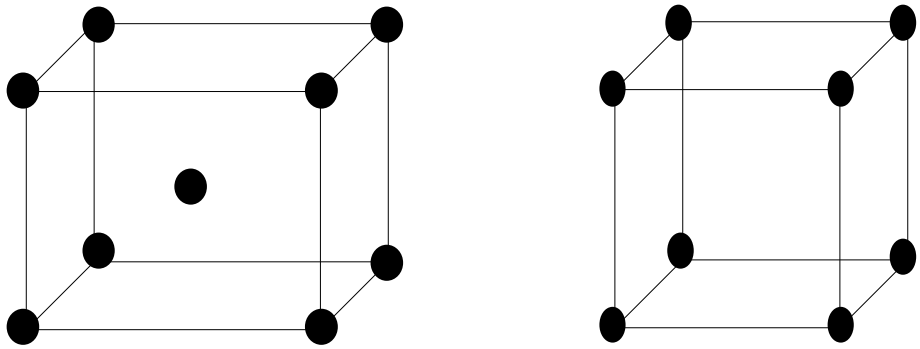

Figure 3.3. BCC and tetragonal structures of tantalum.

Tantalum can form oxides such as Ta_2O_3, TaO and Ta_2O_5. Tantalum pentoxide is the most stable phase with high dielectric constant (~ 25) and it is generally used in multichip module and DRAM applications. In this thesis, we use it as an insulating barrier layer because barrier height of Ta_2O_5 is lower (~0.4 eV) than the other barrier layers, which allows to increase barrier thickness, hence reduce the magnetostatic coupling. It also results in low resistance area product (RxA).

CHAPTER 4

EXPERIMENTAL TECHNIQUES

In this chapter, the growth and characterization techniques will be discussed. All the layers were grown in a UHV magnetron sputtering system. The structural properties were studied by X-ray powder diffraction (XRD), and atomic force microscopy (AFM). Magnetic properties were studied by vibrating sample magnetometer (VSM). Ellipsometry was used to study the properties of the TaO_x insulator layer. Electrical and magnetoresistance measurements were performed by four point probe technique.

4.1. Magnetron Sputtering System

Sputtering technique is one of the most commonly used methods for thin film deposition. When a solid surface is bombarded by energetic particles such as ions, it is seen that surface atoms of the solid are removed from the surface because of the collision between the ions and the surface atoms. This phenomenon is known as sputtering. In a sputtering system, a potential difference is created between the target and substrate and the target is hold generally in the negative voltage. Then, the ionized Ar gases (Ar^+) are accelerated towards the target under an electric field. After that, Ar^+ ions transfer their kinetic energies to the surface atom by collision and the surface atoms ejected from the target and stick on the substrate surface, resulting in growth of films. In the magnetron sputtering system, magnets are placed under the target in order to trap the electrons created in the sputtering process and to increase the ionizing probability. The Figure 4.1 shows the schematic magnetic configuration of a magnetron head.

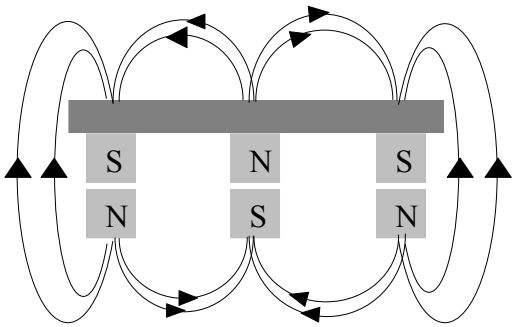

Figure 4.1. Magnet configuration and magnetic field lines of a magnetron head

Depending on the electrical properties of the materials DC or RF sputtering can be used. DC sputtering is used for conductors while RF sputtering is used for insulators. The only difference between DC and RF sputtering is that a high frequency (13.56 MHz) rf power supply is used instead of dc power supply. It electrically reverses the anode and cathode in order to prevent the accumulation of positive charges on the insulator target.

In this study, all single and multilayers were grown by ATC Orion 5 UHV Magnetron Sputtering System shown in Figure 4.2. The system is computer-controlled and has 2" magnetron sources. The load-lock chamber is used for sample preparation. The base pressure is about $5x10^{-8}$ Torr and dc and rf sputtering can be done with the maximum powers of 500 W and 300 W, respectively. The system also allows heating the samples up to the 850 °C by using a halogen lamp based heater.

Figure 4.2. ATC Orion 5 UHV Sputtering System.

4.2. Characterization Techniques

4.2.1. X-Ray Diffractometer (XRD)

X-ray diffractometer is the most commonly used method for determining the crystalline structure of materials. The typical crystalline properties of samples are obtained by using Bragg's law ($2d\sin\theta = n\lambda$) as shown in Figure 4.3. According to the Bragg's law, lattice parameter for a cubic crystalline is given by following equation.

$$a = \frac{\lambda}{2\sin\theta} \cdot \sqrt{(h^2 + k^2 + l^2)}$$

where h, k and l are the miller indices. The lattice parameters are identical for all crystalline materials.

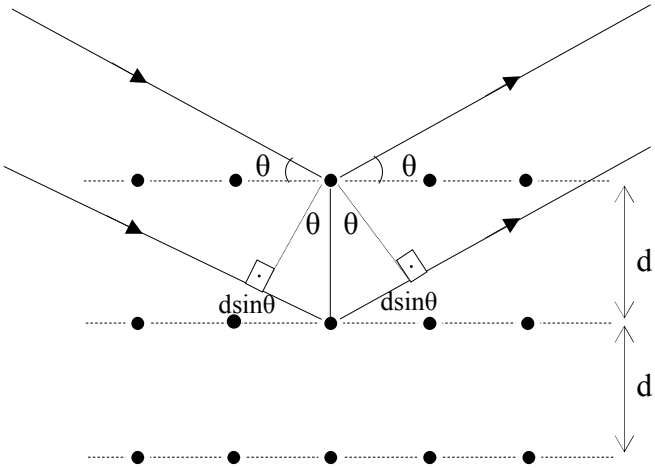

Figure 4.3. X-ray diffraction

Crystalline structure and quality of a given material can be understood from the diffraction peaks. The intensity, position and FWHM (full width at half maximum) of the diffraction peaks are used to determine that properties. The FWHM is calculated by the following formula and is shown in Figure 4.4.

$$B = \frac{1}{2} \cdot (2\theta_1 - 2\theta_2)$$

where $2\theta_1$ and $2\theta_2$ represent the points which the X-ray diffraction peak reach the zero. Grain sizes can calculated from the related X-ray peak by using the Scherer's formula,

$$D = \frac{K\lambda}{B\cos\theta_B}$$

where λ is wavelength of the x-ray, B is the FWHM of diffraction peak, θ_B is the diffraction angle and K is a constant, which is about 0.9. In this study, all XRD measurements were perform by Philips X'Pert Pro X-ray diffractometer using a Cu Kα X-ray source (λ=0.154 nm) in the powder method

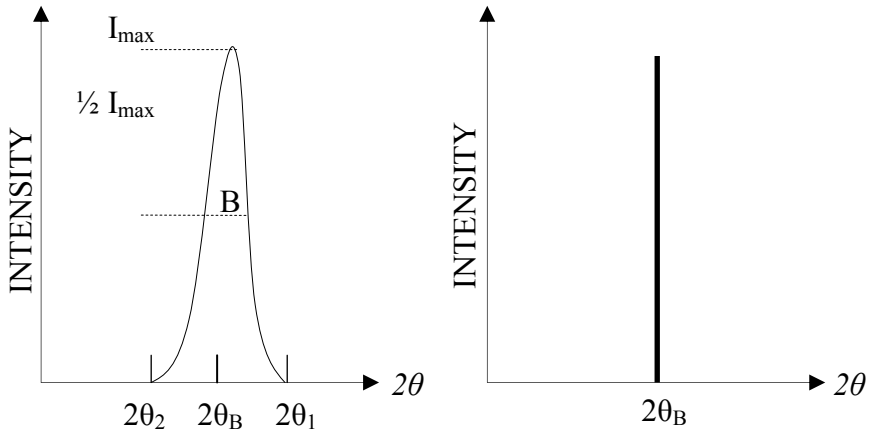

Figure 4.4. a) FWHM for a real and b) ideal XRD peak (Cullity and Stock 2001)

4.2.2. Atomic Force Microscopy (AFM)

Atomic force microscopy is one of the most useful method for observing the surface topographic images of thin films. An AFM consists of a micron size cantilever and a silicon based tip attached on the cantilever. When the tip scans a surface, the cantilever moves up and down depending on the interaction between the tip and sample surface. Then, a laser beam is sent on the cantilever in order to detect the deflection of the reflected beam. Next, reflected laser is detected by a photodiode and topographic images are observed. In this study, Multiple SPM (NT-MDT Solver Nova Tech.) device was used to study the sample surfaces and measuring the roughness of the surfaces. All measurements performed in the tapping mode.

4.2.3. Ellipsometry

Ellipsometry is an optical technique for measuring the thickness and dielectric properties of materials. The working principle depends on the change of the polarization of incoming light. An electromagnetic beam is emitted from a light source, HeNe laser with 632.8 nm wavelength, and linearly polarized and focused on the sample surface. Then, it is reflected from the surface and there exists a change in its polarization. After that, changing polarization of the reflected radiation which is

proportional to the sample properties such as thickness and refractive index is measured by a detector. This method is useful for thin film experiments.

In this study, we used Sentech SE801-E spectroscopic ellipsometry only to measure the refractive index of TaO_x insulating layer.

4.2.4. Vibrating Sample Magnetometer (VSM)

Vibrating sample magnetometer is used to measure the magnetic properties of magnetic samples. It consists of an electromagnet, a mechanically vibrating head and sensing coils. The basic working principle depends on the Faraday's law. When a magnetic sample is placed within a uniform magnetic field, a magnetic moment, m, will be induced in the sample. Then, the sample is forced to make a sinusoidal motion. Thus, an induced voltage occurs in the sensing coils due to the changing magnetic flux. This voltage is proportional to the magnetization of the sample. The induced voltage in the sensing coils is given by,

$$V = mAfS$$

where m is magnetic moment, A is amplitude of vibration, f is frequency of vibration and S is sensitivity of sensing coils.

In this study, Lakeshore 7407 Vibrating Sample Magnetometer shown in Figure 4.5 was used. The moment sensitivity at the ambient temperature is 0.1 μemu and maximum limit at that temperature is 1000 emu. The vibrating frequency is 84 Hz.

Figure 4.5. Lakeshore 7407 Vibrating Sample Magnetometer

4.2.5. Electrical and Magnetoresistance Measurements

Electrical measurements were done by conventional four-point probe technique. A Keithley 2400 source meter and an I-V program written in labview were used for this purpose. To connect the Keithley source meter to computer we also used Agilent connection program for GPIB connection cable. After the connection between the devices, electrical current was used as a source and voltage was sensed. Current was increased from *-1 μA* to *1 μA* and the step range was *10 nA*. Figure 4.6 shows I-V program used in this experiment.

To find the effective barrier height and thickness of the insulator the column of I was divided by the area of junction and J-V curve was plotted. Then this curve was fitted to the Simpson's tunnel equation. Firstly, an arbitrary barrier height and thickness were chosen and then curve fitted to the experimental data by changing the barrier height and thickness.

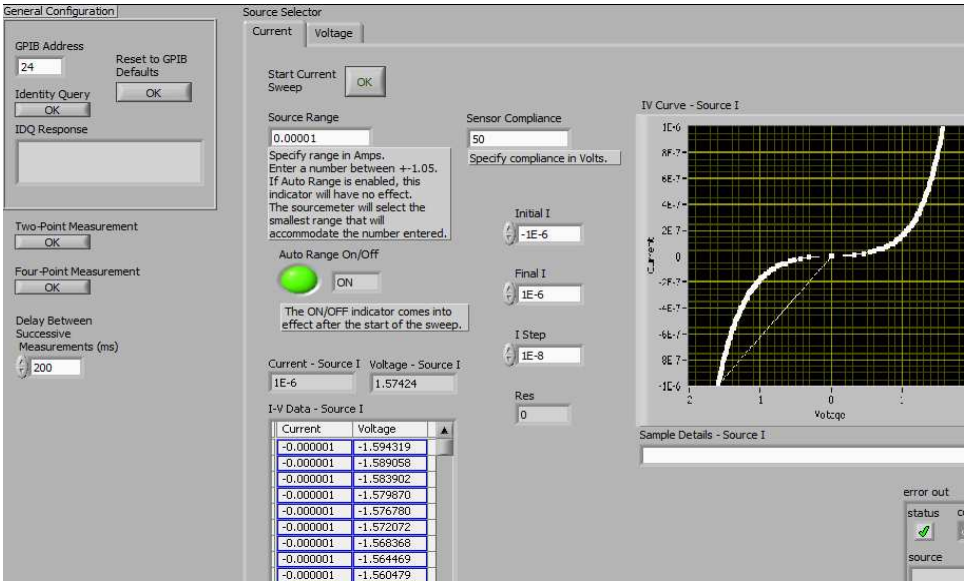

Figure 4.6. Program used for I-V measurements

Magnetoresistance measurements were also performed by a labview program. Like I-V, the same connections were done for magnetoresistance measurements and sample was putted between the magnetic poles. External field was applied from 1000 Oe to -1000 Oe or larger scale to achieve the completely parallel magnetization of two magnetic electrodes and bias voltage applied in the order of a few mV (1mV-10mV).

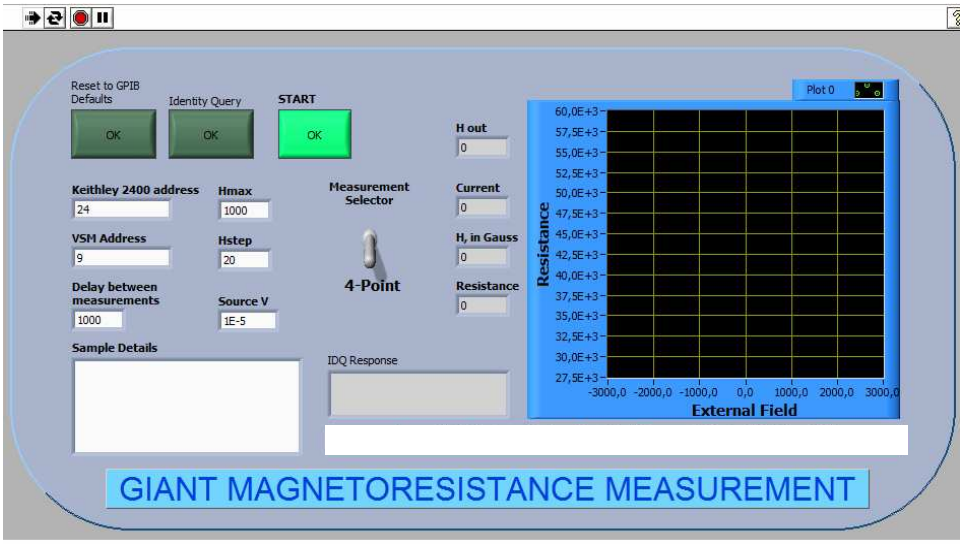

Figure 4.7. R-H program for magneto resistance measurements

CHAPTER 5

RESULTS AND DISCUSSION

In this chapter, the relationships between magnetic and structural properties of the magnetic multilayers and single layers will be discussed. It is well known that magnetic properties of magnetic films strongly depend on the structural properties (Ng, et al. 2002). Therefore, XRD and AFM analysis will be a key to understand the magnetic behaviors.

5.1. X-Ray Diffraction Results

5.1.1. SiO_2/Fe

Figure 5.1 shows the XRD pattern of the various thickness of Fe grown on SiO_2. There is no visible peak for 6 nm Fe. However, when the thickness of the Fe layer increases, the peak of Fe bcc (110) orientation appears at 2θ value of 44.96 degrees. The intensity of this peak increases with increasing Fe thickness. The FWHM is 0.85° and the corresponding grain size is 10.1 nm. When the thickness of the Fe film reaches to 72 nm, the FWHM decreases to 0.53° and grain sizes increases to 16.1 nm. The XRD data also show a shift in the Fe peak with increasing thickness. Calculated lattice parameters are 2.851 Å and 2.865 Å for 12 and 72 nm Fe films, respectively. This indicates the presence of a small strain in the thinner films, however the strain disappears for the thicker film and lattice constant are close to the bulk Fe lattice parameter.

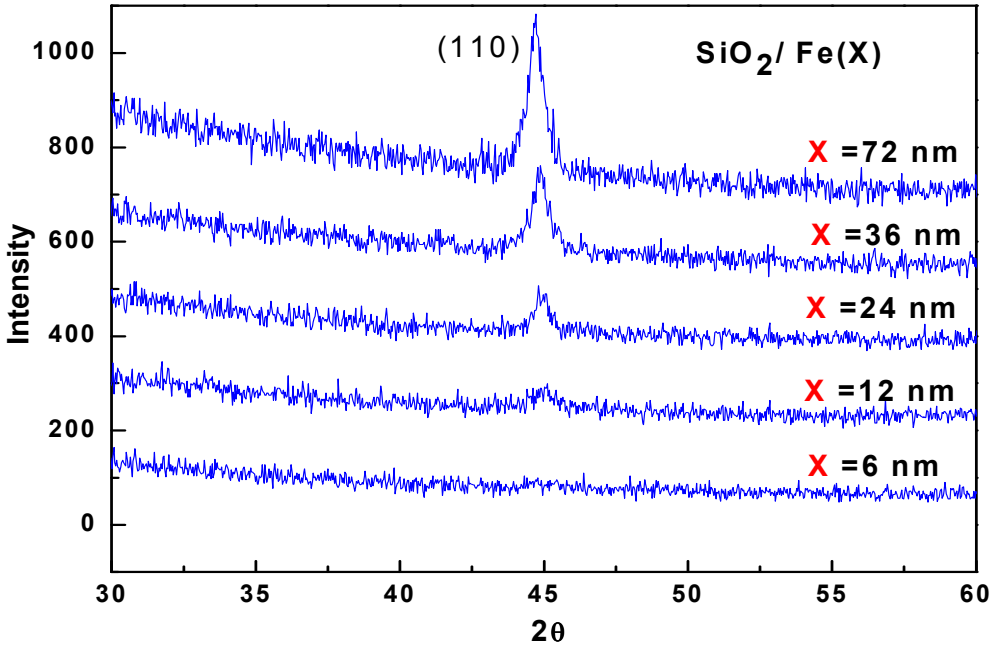

Figure 5.1. The XRD patterns of Fe films for various thicknesses

5.1.2. SiO_2/Ta/Fe

In order to see the effect of Ta on the structure of Fe film, Ta buffer layer was grown on the SiO_2 substrate. Figure 5.2 shows the XRD pattern of 12 nm Fe grown on 24 nm Ta. There are two sharp peaks: bcc Fe (110) at 44.42°and β-Ta (200) at 33°. When the Fe (110) peak is compared with the 12 nm Fe peak in the figure 5.1, it is seen that Ta buffer layer increases the crystalline quality of Fe. The reason may relate to the growing Fe on a crystalline Ta structure and hence it gains a crystalline order easily. The calculated grain size and FWHM are 14.9 nm and 0.55°, respectively. Also the calculated lattice parameter is 2.881 Å, which indicates the existence of a strain in the Fe film. It can be inferred that the growth conditions and structure of buffer layer strongly affect the structural properties of the magnetic thin films (Park, et al. 2002).

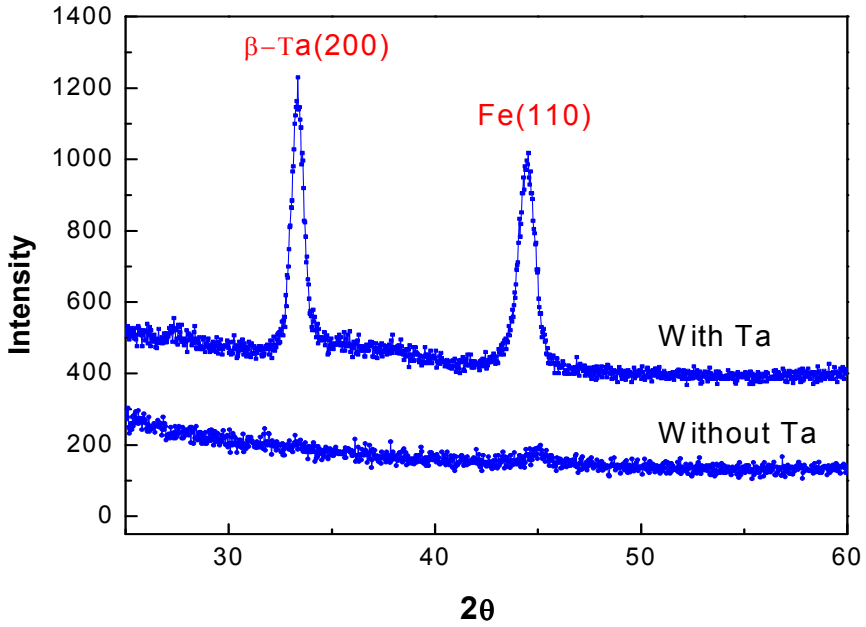

Figure 5.2. The XRD pattern of Ta(24nm)/Fe(12nm) and Fe (12nm) grown on SiO_2.

5.1.3. SiO_2/Ta/Fe/TaO_x

In this part, we will determine the effect of thickness of the Ta buffer layer on the structural property of Fe films. We grew SiO_2/Ta(d)/Fe(6nm)/TaO_x(5nm) structures with substrate bias cleaning as a buffer layer in order to see how the crystallinity of the Fe films change. Figure 5.3 shows the XRD pattern of the Fe film with different Ta under layer thickness. For 6 nm Ta buffer layer, a small Fe (110) peak is seen at 44.713°. However, intensity of this peak is very small and broad. The FWHM is 4.001° and grain size is 2.1 nm. When the thickness increases to 12 nm, a clear Fe peak is observed at 44.567.° The FWHM is 1.086° and corresponding grain size is 8 nm. Furthermore, increasing Ta thickness causes gradual reduction of the Fe peak. The reason may be associated to the structural changes of Ta as the thickness increases.

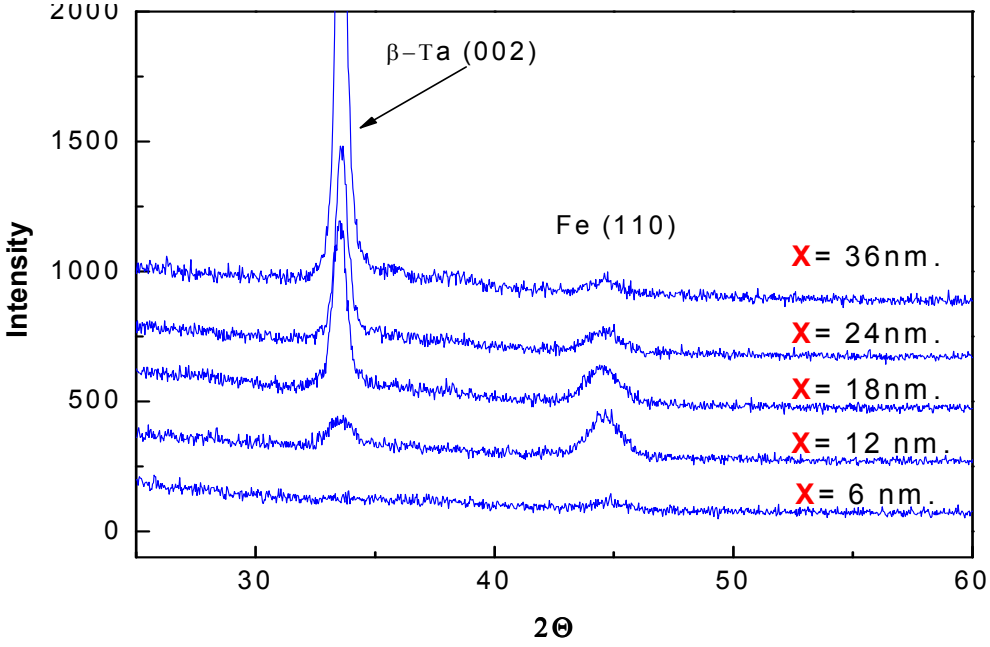

Figure 5.3. XRD pattern of Fe film with various buffer layer thicknesses.

5.2. Atomic Force Microscopy Results

In order to observe the surface morphology and roughness analysis, which are important parameters for magnetic interlayer coupling, 3D AFM images of Ta and Fe layers were investigated. The scanned areas for all samples are 5x5 μm^2. The surface roughness of SiO_2 substrate is 2 Å. It is atomically smooth. The roughness of the substrate is important because it affects the over layer growth strongly.

5.2.1. SiO_2/Ta

The surface morphology of Ta films on SiO_2 substrate with various thicknesses (6, 12, 18, 24 and 36 nm) was investigated. Figures 5.4 and Figure 5.5 shows the surface morphology of 6 and 36 nm thick Ta films, respectively. The corresponding roughnesses of Ta and Fe films with various thicknesses were shown in figure 5.6. is seen that Ta film has quite smooth and uniform surface structure on SiO_2 substrate. The roughness is increasing at the beginning and then formation of continuous structure results in a decrease in the roughness. Then, it increases again with increases thickness. The maximum rms roughness was found to be ~2.36 Å for 36 nm thick Ta. These results are desirable for obtaining smooth interfaces of MTJs.

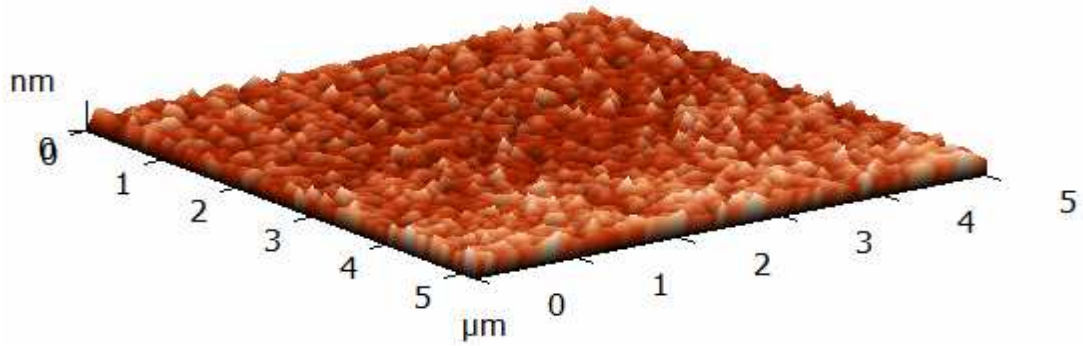

Figure 5.4. AFM images of 6 nm thick Ta thin film. Rms roughness is 2.3 Å

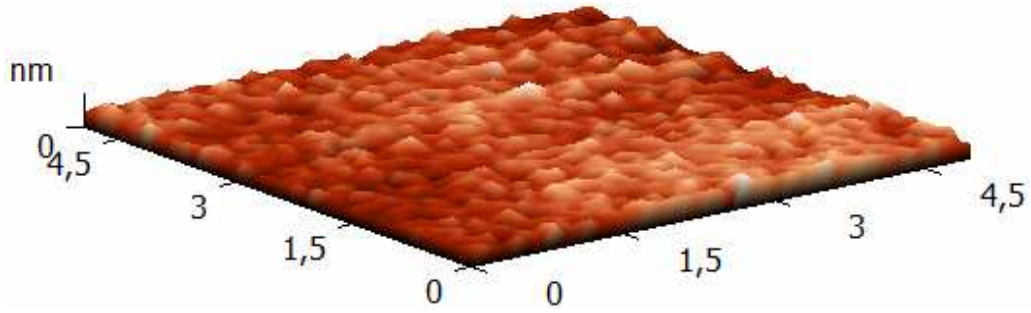

Figure 5.5. AFM images of 36 nm thick Ta thin film. Rms roughness is 2.4 Å

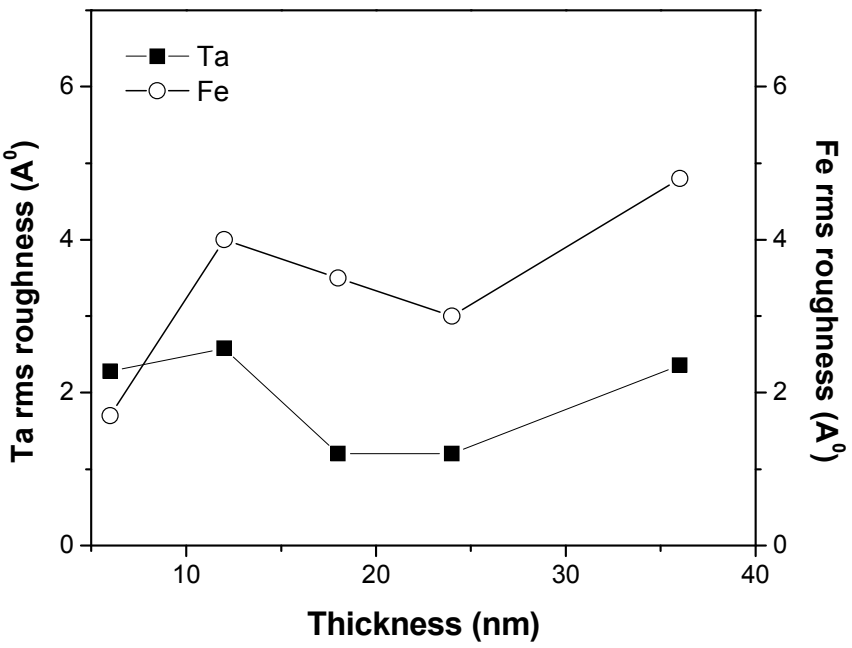

Figure 5.6. Rms roughness of SiO_2/Ta and SiO_2/Fe single layers

5.2.2. SiO_2/Fe and SiO_2/Ta/Fe

Figures 5.7 and 5.8 show the surface topographic images of Fe films for 12 nm and 72 nm thicknesses. For the 6 nm Fe film, the rms roughness was found to be 1,7 Å and then it increases 4 Å for the 12 nm thick Fe film. Like the Ta film, rms roughness decreases after the 12 nm thick Fe film and then it increases gradually. The reason for this change can be related to the fact that increasing thickness until at a certain thickness results in disappearing defects and inhomogenities (Entani, et al. 2005). Furthermore, Fe film on SiO_2 substrate starts to crystallize after the thickness of 12 nm. Existing crystalline structure causes an increase in grain sizes and releasing the stress in the film. Therefore, surface roughness reduces. Figure 5.6 also shows the rms roughness of SiO_2/Fe structures. The effect of Ta under layer on the surface roughness of Fe is shown in figure 5.9. The rms roughness of 12 nm Fe film with 24 nm Ta under layer was found to be 1.2 Å. Ta reduces the roughness of 12 nm Fe film from 4 Å to 1.2 Å. This can be related to the increasing of structural properties of Fe film, resulting in an increasing grain sizes.

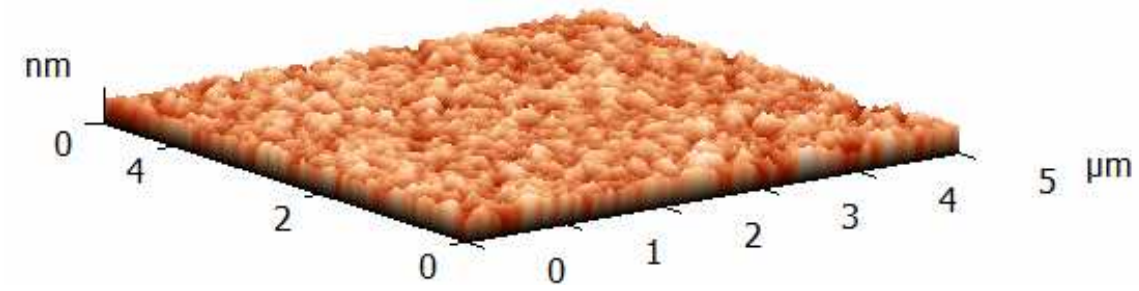

Figure 5.7. AFM images of 12 nm Fe film on SiO_2 . Rms roughness is 4 Å

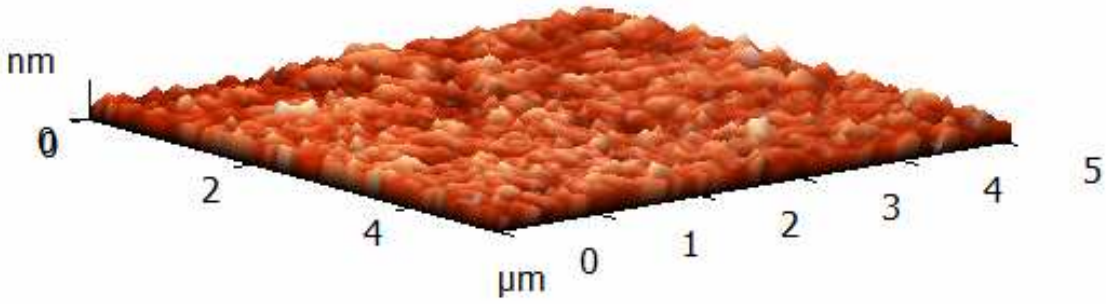

Figure 5.8. AFM images of 72 nm Fe film on SiO_2 . Rms roughness is 6.3 Å

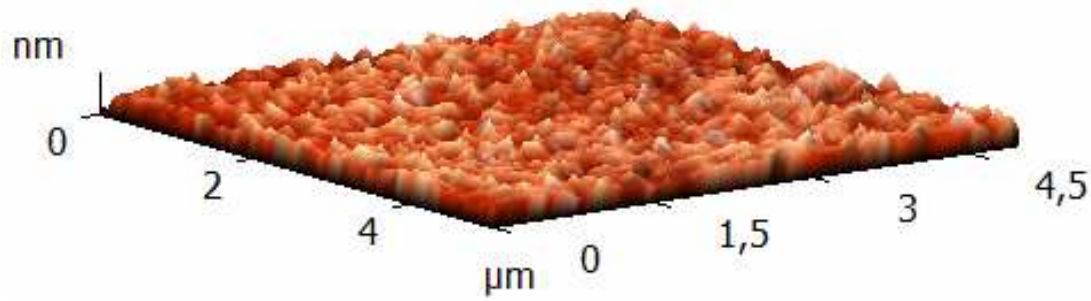

Figure 5.9. AFM images of Ta(24nm)/Fe(12nm) on SiO_2. Rms roughness is 1.2 Å

5.3. Vibrating Sample Magnetometer

5.3.1. SiO_2/Fe

Magnetic hysteresis loops of Fe layer with different thicknesses on SiO_2 substrate are shown in the Figure 5.10. When the thickness of Fe film increases, the H_c increases linearly. This result may be related to the increase of grain sizes with the thickness of Fe layer as can seen from the XRD measurements. It is well known that if the grain sizes increase, crystalline magnetic anisotropy increases within the each grain and magnetization of each grain has a different orientation. In this case, magnetization can not rotate at the same time causing an increase in the H_c for thicker films (Sharma, et al. 2005).

The hysteresis loops are nearly square like shape and there is no magnetic anisotropy indicating that magnetization reversal occurs via the domain walls motion (Kumar and Gupta 2006, Swerts, et al. 2004). If coercivity is associated with domain walls motion across the grain boundaries, than large grain sizes should results in low H_c. However, we observed opposite results for Fe films. Large grains within the Fe films are isolated and grain boundaries play a pinning effect on the domain wall motions. They also cause the disappearance of the anisotropy.

For the 72 nm thick Fe, it is expected that surface roughness increases with increasing thickness and pinning effects on the domain wall motion increases. In the case of rough surface, magnetic poles are induced and in-plane demagnetizing field occurs. This can cause a change in the thickness and sizes of domains. Step edges as a result of rough surfaces also restrict the wall motion. In the magnetization reversal process, external field not only overcomes the domain wall but also overcomes the demagnetizing field. Therefore, domain wall pinning exists and H_c increases (Ng, et al. 2002).

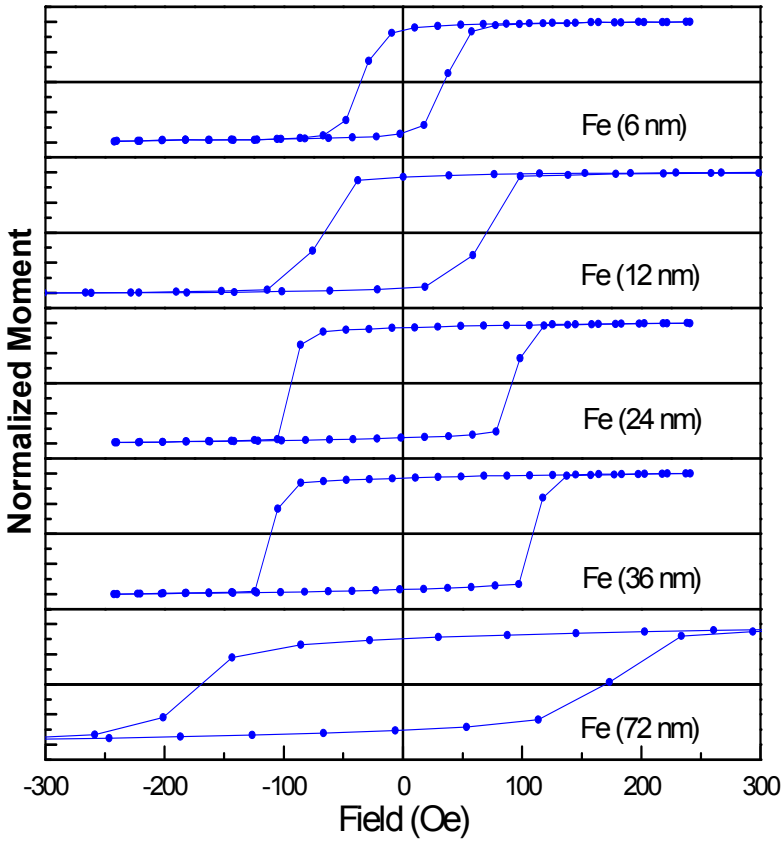

Figure 5.10. The hysteresis loops of Fe thin film with different thicknesses on SiO_2

5.3.2. SiO_2/Ta/Fe

Figure 5.11. shows the effect of Ta buffer layer on the magnetic properties of Fe film. It is seen that Ta buffer layer causes a significant increase, more than three times, in H_c of 12 nm thick Fe film. When the crystallinities of the two layers are compared, this significant increase can be attributed to the improvement of crystalline quality of the Fe layer because of the Ta buffer layer. As it was discussed above, increasing of crystalline quality results from the increasing grain sizes and large grains have large magnetic anisotropy. In this case, each grain has an intrinsic magnetization which does not interact with the other grains and magnetization reversal process occurs independently, resulting in an increase in the H_c. Also the strain in the Fe film causes an increase in the H_c.

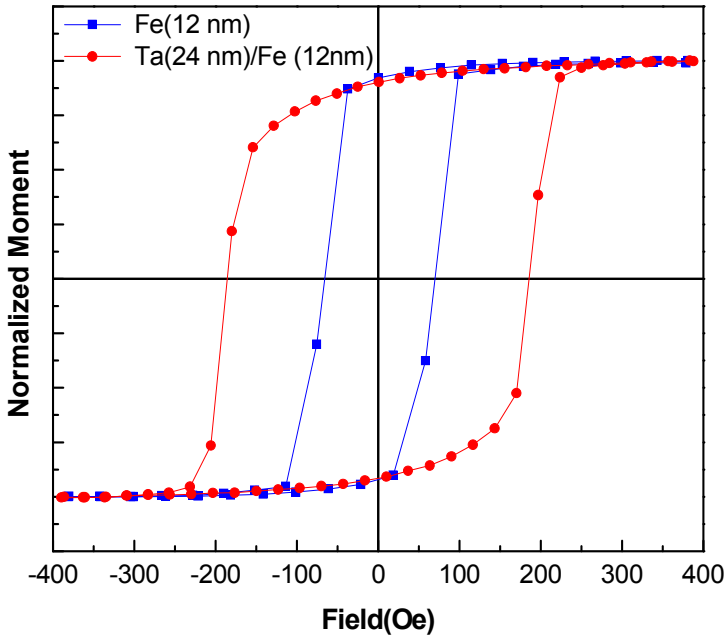

Figure 5.11. The effect of Ta buffer layer on the magnetic properties of Fe layer

5.3.3. SiO_2/Co and SiO_2/Ta/Co

In this case, to see the effect of Ta under layer on the Hc of Co film, 8 nm Co film were grown on the SiO_2 substrate and 24 nm Ta. Figure 5.12 shows the hysteresis loops of 8 nm Co film on SiO_2 substrate. The loops have s-like shapes and there is a small magnetic anisotropy. H_c changes from 45 to 55 Oe. On the other hand, Co film shows large magnetic anisotropy when it is grown on Ta film and H_c reduces to 35 Oe as shown in Figure 5.13. There is a big fluctuation in the squareness. This may be associated to the fact that Ta under layer causes a structural change in Co film and induces a magnetic anisotropy.

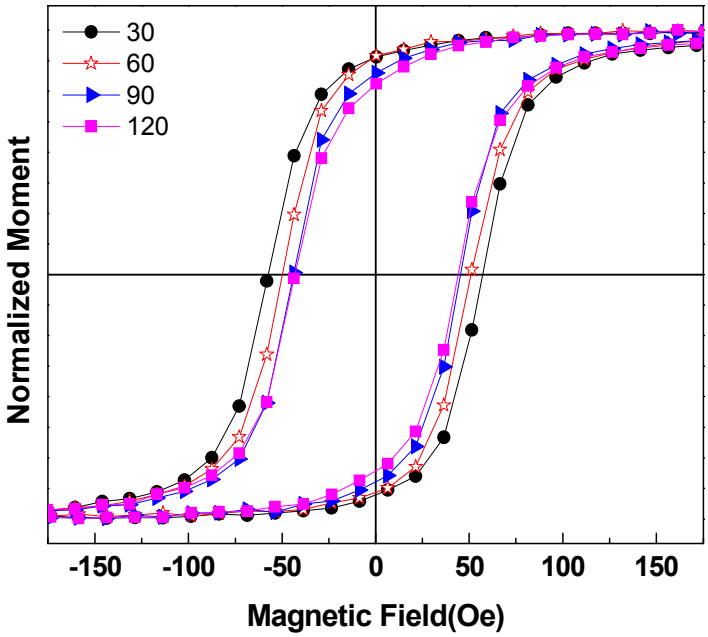

Figure 5.12. The angle dependent hysteresis curves of SiO_2/Co(8nm)

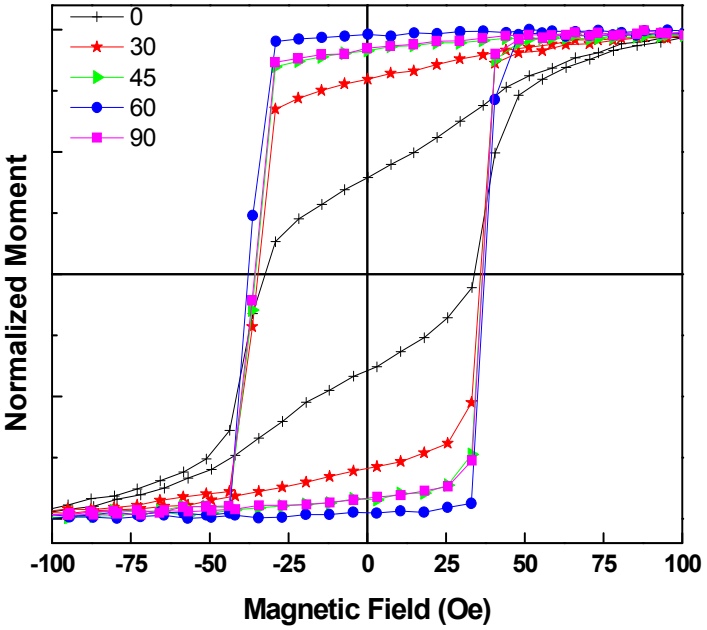

Figure 5.13. The angle dependent hysteresis curves f SiO_2/Ta(24nm)/Co(8nm)

5.3.4. SiO_2/Ta/Fe, SiO_2/Ta/Fe/Ta and SiO_2/Ta/Fe/TaO_x

After determination of the effect of Ta buffer layer, Ta and TaO_x layers were grown on the SiO_2/Ta(24nm)/Fe(12nm) structure in order the observe the effect of TaO_x layers on the magnetic properties of the Fe film. Figure 5.14 shows the hysteresis loops of Ta/Fe, Ta/Fe/Ta and Ta/Fe/TaO_x. When *a* and *b* are compared in Figure 5.14, it is seen that Ta capping layer causes an increase in the H_c of the Fe film from 185 to 218 Oe. The reason is that Ta capping layer prevents the oxidation of the Fe film. The low Hc of the Ta/Fe film arises from the oxidation of the Fe film, resulting in decreasing the crystallinity and grain size of Fe film. This situation is undesirable for MTJs because formation of dead layer at the interfaces can effect the spin polarization of electrons. The *b* and *c* compare the effect of Ta and TaO_x top layers. The TaO_x layer reduces the H_c of Fe film from 218 to 165 Oe, when it is compared with the Ta capping layer. The reduction of the H_c can be related to the oxidation effect as it is explained for the graph *a*. However, the effect of sputtered TaO_x is larger than normal oxidation.

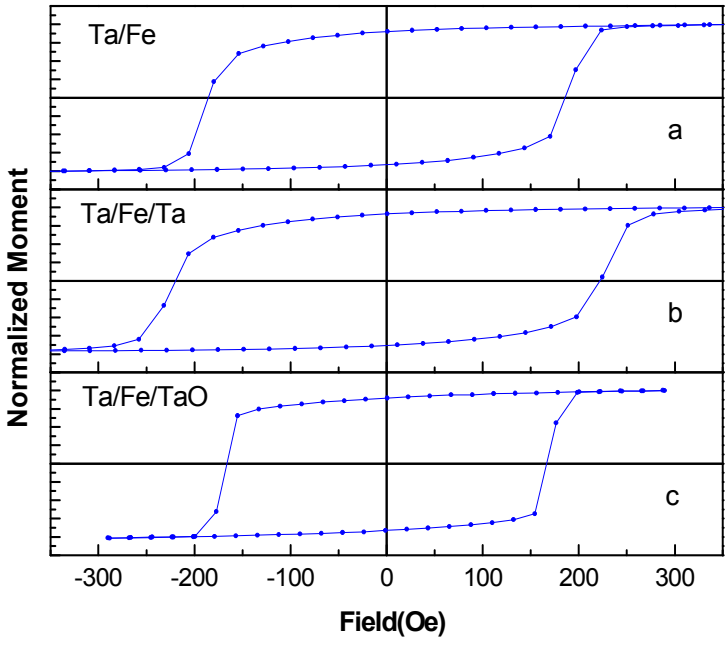

Figure 5.14. The effect of Ta and TaO_x capping layers on the H_c of Fe film

5.3.5. SiO_2/Ta/Fe/TaO_x

In the previous parts, we have investigated the effects of bottom and top layer on the H_c and crystallinity of the Fe film. In this part, we determine the effect of thickness of the bottom Ta buffer layer. We tried different Ta thickness with substrate bias cleaning as a buffer layer. The Figure 5.15 shows the VSM results. The 6 nm Ta layer causes the lowest H_c of the Fe film. However, there is a big jump in the H_c when the thickness of the Ta layer is 12 nm. Then, increasing the Ta layer after that thickness causes a linear decreasing in the H_c. There is no significant change between 24 nm and 36 nm. This can be explained by changes in the structure of Fe film. The 12 nm Ta film creates the best crystalline Fe film with respect to the other. The structural properties of the Fe film strongly affect the magnetic properties.

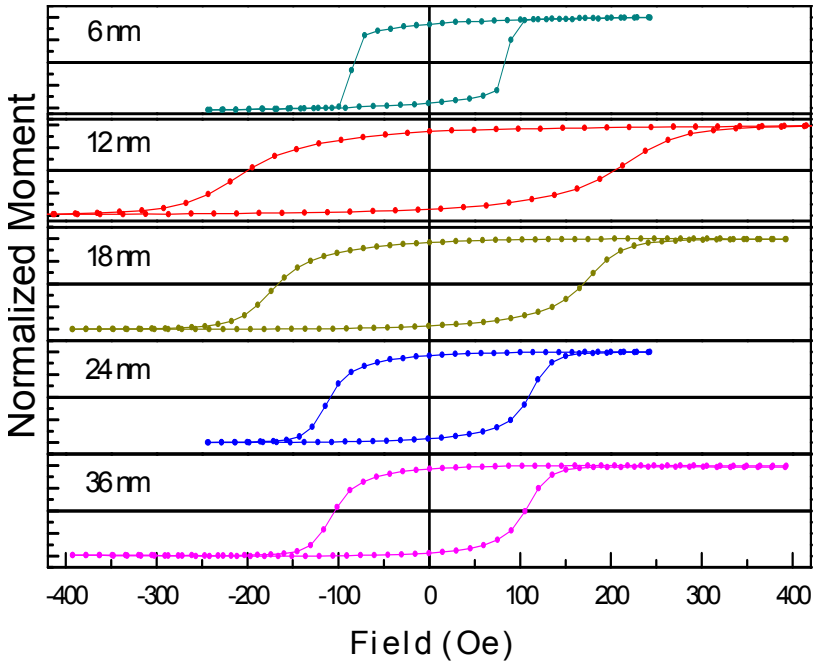

Figure 5.15. Hysteresis loops of SiO_2/Ta(d)/Fe(12nm)/TaO_x(4nm) structure with different Ta buffer layer thicknesses

5.3.6. SiO_2/Ta/Fe/TaO_x/Co

So far we determined the suitable FM layer as a bottom electrode with high crystallinity, high H_c and smooth surface for magnetic tunnel junctions. From now on now, we will investigate the full spin valve structure by growing a cobalt layer as a second FM free electrode. The previous studies show that H_c of the cobalt layer is increasing from 25 to 150 Oe for 5 and 25 nm thickness, respectively. In order to create FM electrodes with different H_c we grew thin Co layers. We grew SiO_2/Ta(24nm)/Fe(12nm)/TaO_x(d)/Co(8nm) layers, where d is the thickness of the insulating barrier grown from Ta_2O_5 target. Figure 5.16 shows the M-H loops of full spin valve structure with different barrier thicknesses of 4, 8, 13 and 18 nm. Magnetic decoupling starts to appear at 4 nm barrier thickness. However, it is very weak. The main reason may be related to the two factors. The first one is that TaO_x is not yet a continuous and uniform structure at that thickness.

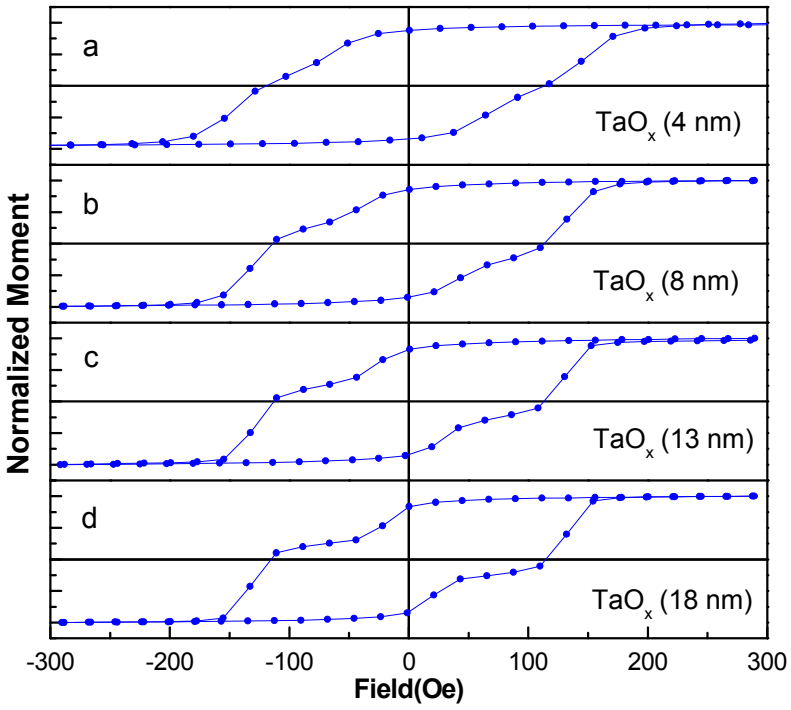

Figure 5.16. The Hysteresis loops of full spin valve stack layer with different TaO_x thicknesses

This results in rough interfaces between the electrodes and allows the interlayer orange-peel coupling. The second reason is that TaO_x does not have the form of Ta_2O_5 which is a good insulator. In this case, conduction electrons in Ta within the barrier can cause an indirect exchange coupling. To clarify the coupling mechanism, minor loops of the whole MTJ stack layer were measured for 4 and 13 nm barrier thicknesses while the hard layer remains in the remanent state. In addition to this, the ellipsometry measurements were done for 5 nm and 10 nm TaO_x in order to determine the quality of oxide layer. Figure 5.17 shows the ellipsometry results of 5 and 10 nm of TaO_x films grown on SiO_2 substrate. Refractive index of 5 and 10 nm TaO_x is ~ 2.6 (at 632.8 nm). However, its ideal value must be between 2.1 and 2.4 for perfect amorphous Ta_2O_5. From these results, we can conclude that our TaO_x is not formed as Ta_2O_5 and it is not a good insulator.

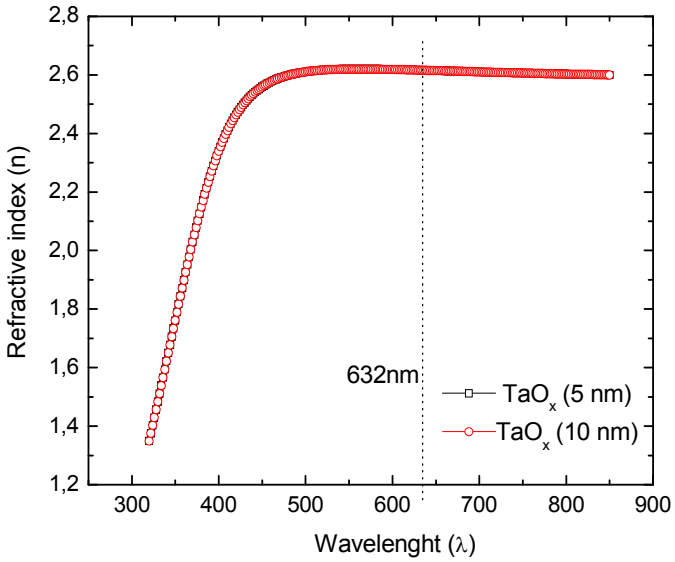

Figure 5.17. Ellipsometry measurements of TaO_x single layers

Then, small decoupling in the 4 nm results from the interlayer exchange interaction as it is discussed in the second explanation. As the barrier thickness increases, clear steps are seen in the M-H loops. For 18 nm TaO_x thickness the magnetic layers are totally decoupled. However, such big thicknesses are not desirable, when the tunneling is considered. Figure 5.18 shows the minor loops (complete hysteresis loop of the free layer) of the Co layers measured in each MTJ stack layer while magnetization of the fixed layer remains in the remanent state. The figure shows the corresponding minor

loops of the Co layer. There is a strong shift in the minor loop of TaO_x (4 nm) indicating strong magnetostatic Néel coupling field of H_N =24 Oe due to the correlated interface roughness of the two ferromagnetic electrodes at the barrier. The further increase of the barrier causes a reduction in the coupling field in the value of 16, 8 and 5 Oe for 8 , 13 and 18 nm, respectively. The larger coupling field is expected for small barrier because the Néel coupling field is increases exponentially with decreasing barrier thickness.

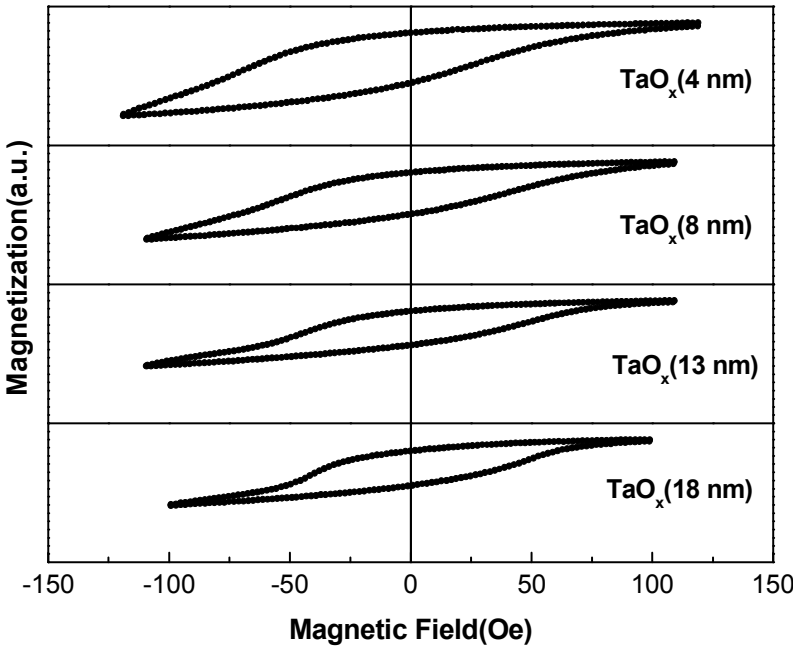

Figure 5.18. The minor loops of Co free layer on the Full MTJ stack layers

For the small barrier thicknesses, it is hard to determine the contributions of each layer to the total magnetization because not all of the Co moments had reversed before the moments of Fe switched. The H_c of Co was about 44 Oe (at the inflection point) for MTJ stack layer with TaO_x (4 nm) and it decreases to 41, 38 and 35 Oe for the barrier thicknesses of 8, 13 and 18 nm, respectively. Also sharper switching behavior is observed with increasing thickness. The reason of larger H_c for small spacer may be related to lock-in of stray fields, generated by domain walls and magnetization ripple in Co layer, by the fixed layer stray fields associated with domain walls and magnetization ripple in the fixed layer (Chopra, et al. 2000).

5.4. Annealing Effect on SiO_2/Ta/Fe/TaO_x/Co

After determining the effect of Ta buffer layer and barrier thickness on the evolution of magnetic decoupling, we studied the annealing effect on the whole stack layers. Figure 5.19 shows the M-H loops for different annealing temperatures of SiO_2/Ta(24nm)/Fe(12nm)/TaOx(13nm)/Co(8nm). it is seen that annealing results in a strong change on the hysteresis loops. H_c of Fe film increases with increasing temperature until the 400°C and antiparallel field range, width of the plateau on the figure, increases. Annealing at low temperatures causes an increasing of grain sizes and crystallinity of Fe film resulting in an increase in the H_c and also the Fe/TaO_x interface becomes smooth because of oxygen redistribution at the interface and TaO_x has a homogeneous structure, decreasing magnetostatic coupling (Lee, et al. 2002). However, there is a sharp decrease in the H_c of Fe film after that temperature and the plateau in the antiparallel region becomes rounder. The reason can be related to the strong interdiffusion at the interface for higher annealing temperatures (Lin, et al. 2002). This results in formation of FeO_x and CoO_x dead layers which cause the spin flip scattering and low TMR ratio at the interface and a shortcut between the magnetic layers.

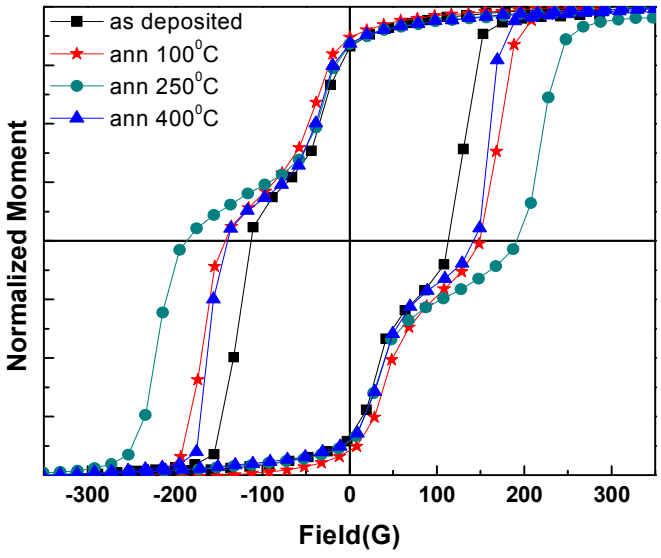

Figure 5.19. Hysteresis curves of SiO_2/Ta(24nm)/Fe(12nm)/TaO_x(13nm)/Co(8nm) stack layers

5.5. Electrical and Magnetoresistance Measurements

In this part, electrical and magnetoresistivity measurements of whole MTJ stack layer will be explained. For this purpose, 100x100 μm^2 MTJ's were fabricated by using conventional photolithography technique.

Figure 5.20 shows the I-V characteristics of SiO_2/Ta/Fe/TaO_x(13nm)/Co/Ta MTJ stack layer. From the figure it can be seen that conduction is supplied by the tunneling electrons and there is no any conduction bridge within the insulating layer. Then, the I-V curve was fitted to the Bringman's tunnel equation to find the effective barrier height and barrier width as shown in Figure 5.21. From the graph, effective barrier height and barrier thickness were calculated as 1.45 eV and 1.88 nm, respectively. There are big differences between expected barrier height and barrier width. The large barrier width may be related to the formation of sub-tantalum oxide according to the ellipsometry results.

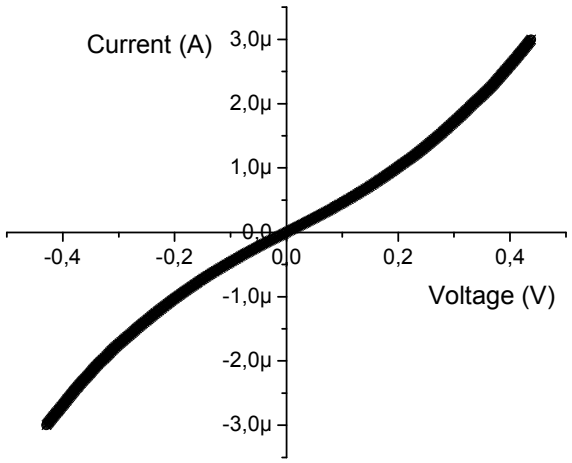

Figure 5.20. Non-linear I-V characteristics of SiO_2/Ta/Fe/TaO_x(13nm)/Co/Ta MTJ stack layer

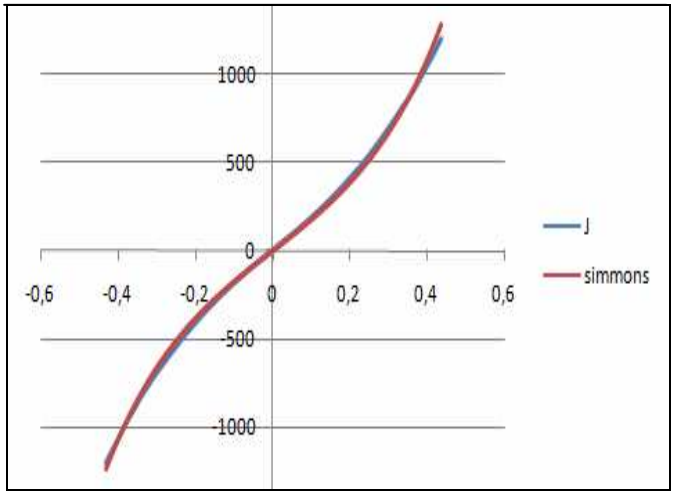

Figure. 5.21. Fitted J-V curve of SiO_2/Ta/Fe/TaO_x(13nm)/Co/Ta MTJ stack layer.

Magnetoresistance measurements were done under an external magnetic field. However, none of the junction showed a measurable magnetoresistance effect at room temperature. The possible reasons may related to the formation of sub-tantalum oxide, dirty interfaces from the lithography or formation of FeO_x dead layer at the interfaces.

CHAPTER 6

CONCLUSIONS

In this study, structural and magnetic properties of SiO_2/Ta/Fe/TaO_x/Co multilayer were studied. To build up a good magnetic multilayer, Fe, Co, Ta/Fe, Ta/Co, Ta/Fe/TaO_x single and multilayers were investigated by AFM, XRD, VSM and ellipsometry characterization techniques. Then electrical and magnetoresistance measurements were done by conventional four point probe technique.

XRD results showed that Fe film starts to gain crystalline order at 12 nm thickness on SiO_2 substrate and its crystallinity increases with increasing thickness. Using 24 nm Ta buffer layer causes large increase in the crystallinity of Fe peak. The crystallinity of the Ta under layer also affects the structural and magnetic properties of Fe film.

AFM results showed that Fe films have very smooth surfaces and their rms roughness change from 1.7 Å to 6.3 Å for the thicknesses between 6 nm and 72 nm. For small thicknesses roughness first increases up to 4 Å and then decreases with increasing thickness. This shows the formation of uniform film and transition from amorphous phase to crystalline structure. For larger thicknesses, rms value increases with increasing thickness. The same situation was seen in the Ta buffer layer.

VSM measurements showed that magnetic properties of magnetic films were strongly affected by structural properties of the films. H_c of Fe film increased with increasing thickness. When it was compared with the XRD data, it was seen that H_c of Fe film strongly depended on the crystalline structure. Furthermore, the films did not show any magnetic anisotropy. This shows that the magnetization reversal is dominated by domain walls motion. Formation of crystalline structure caused domain wall pinning centers at the grain boundaries. This caused the disappearance of the anisotropy within the films. Moreover, magnetic properties of films also were strongly affected by crystalline structure of under layer.

To see the oxygen effect on the H_c of Fe film, TaO_x and Ta capping layers were grown on Fe films and they were compared with the as-deposited Fe film (oxidized with air). The results indicated that the Hc of Fe film was smallest one with TaO_x

capping layer film while the Ta capping layer made the highest Hc of Fe. It was concluded that there was oxygen diffusion into the Fe layer resulting in reduction of crystallinity. When the coercivities of as deposited and TaO_x capping Fe films compared, we saw that the effect of oxygen diffusion was higher in the case of Fe/TaO_x.

Co minor loops showed that there is strong magnetostatic coupling between FM layers. The strength of coupling is large for thin TaO_x barrier and it is small for thicker TaO_x. The reason can be related to the formation of non-uniform and sub tantalum-oxide instead of Ta_2O_5 as well as large Neel orange peel coupling.

Annealing of the MTJ structure improves the magnetic decoupling and Hc of Fe. However, when the temperature reached to the 400°C, there was a strong reduction in both H_c of Fe and decoupling mechanism. The reason was associated with the increasing annealing temperature increases the crystalline quality of Fe up to the 250 °C and increases the H_c of Fe. Also annealing causes the formation of smooth interface, resulting in a decrease of the orange-peel coupling. In contrast, higher annealing temperatures cause the oxygen diffusion between Fe and TaO_x interfaces. Therefore, FeO_x dead layer may exist at the interface, which causes the reduction in H_c of Fe.

Finally, 100x100 μm^2 MTJs were fabricated by conventional photolithography technique. Then, electrical measurements showed non-linear I-V characteristics and effective barrier height and barrier width were found 1.45 eV and 1.88 nm, respectively. Magnetoresistance measurements were done under an external magnetic field. However, none of the junctions showed a measurable magnetoresistance effect at room temperature.

REFERENCES

Baibich, M.N., J.M. Broto, A. Fert, Van Dau F. Nyugen, F. Petroff, P. Eitenne, G. Creuzet, A. Friederich, and J. Chazelas. 1988. Giant magnetoresistance of (001)Fe/(001)Cr magnetic superlattices. *Physical Review Letters* 61 (21):2472

Binash, G., P. Grünberg, F. Saurenbach and W. Zinn. 1989. Enhanced Magnetoresistance in layered magnetic structures with antiferromagnetic interlayer exchange. *Physical Review* B 39 (7):4828-4830.

Bowen, M., M. Bibes, A. Barthélémy, J.P. Contour, A. Anane, Y. Lemaitre and A. Fert. 2003. Nearly total spin polarization in $La_{2/3}Sr_{1/3}MnO_3$ from tunneling experiments. *Applied Physics Letters* 82:233-235.

Bowen, M., V. Cros, F. Petroff, A. Fert, C. M. Boubeta, J.L. Costa-Krämer, J.M. Anguita, A. Cebollada, F. Briones, J.M. de Terasa, L. Morellón, M.R. Ibarra, F. Güell, F. Peiró and A. Cornet. 2001. Large magnetoresistance in Fe/MgO/FeCo(001) epitaxial tunnel junctions on GaAs(001). *Applied Physics Letters* 79:1655-1657.

Brinkman, W.F., R.C. Dyness, and J.M. Rowell. 1970. Tunneling conductance of asymmetrical barriers. *Journel of Applied Physics* 45:1915-1921.

Cullity, B.D. and S.R. Stock, 2001. *Elements of x-ray diffraction.* New Jersey: Prentice Hall.

Djayaprawira, D.D., K. Tsunekawa, M. Nagai, H. Maehara, S. Yamagata, N. Watanabe, S. Yuasa, Y. Suzuki and K. Ando. 2005. 230% room-temperature magnetoresistance in CoFeB/MgO/CoFeB magnetic tunnel junctions. *Applied Physics Letters* 86:92502

Entani, S., M. Kiguchi, S. Ikeda and K. Saiki. 2005. Magnetic properties of ultrathin cobalt films on SiO2 substrates. *Thin Solid films* 493:221-225.

Han, X. F., M. Oogane, H. Kubota, Y. Ando and T. Miyazaki. 2000. Fabrication of high-magnetoresistance tunnel junctions using $Co_{75}Fe_{25}$ ferromagnetic electrodes. *Applied Physics Letters* 77:283–285.

Hardley, M. J., R. Atkinson and R. J. Pollard. 2002. Magnetic properties of Co films deposited onto obliquely sputtered Ta underlayer. *Journal of Magnetism and Magnetic Materials* 246:347-350.

Hehn, M., O. Lenoble, D. Lacour and A. Schuhl. 2000. Magnetic anisotropy and domain duplication in transport properties of tunnel junctions. *Physical Review* B 62(17):11344-11346.

Hook, J. R. and Hall, H. E. 1995. *Solid State Physics*. Chicester: John Wiley & Sons.

Jiang, A., T.A. Tyson, L. Axe, L. Gladczuk, M. Sosnowski, P. Cote. 2005. The structure and stability of β-Ta thin films. *Thin Solid Film* 479:166-173.

Jullière, M. 1975. Tunneling between ferromagnetic films. *Physics Letters* 54A(3): 225-226.

Kumar, G. 2004. Structural and magnetic characterization of Nd-based Nd-Fe and Nd-Fe-Co-Al metastable alloys. *Technical University Dresden Thesis of Ph.D*

Kumar, D., and A. Gupta. 2007. Evolution of structural and magnetic properties of sputtered nanocrystalline Co thin films with thermal annealing. *Journal of Magnetism and Magnetic Materials* 308:318-324.

Lee, K. I., J. H. Lee, W.Y. Lee, K.W. Rhie, J. G. Ha, C.S. Kim and Shin K. H. 2002. Enhanced tunneling magneroresistance and thermal stability of magnetic tunnel junction by rapid anneal. *Journal of Magnetism and Magnetic Materials* 239:120-122.

Lee, Y. M., J. Hayakawa, S. Ikeda, F. Matsukura, H. Ohno. 2007. Effect of electrode composition on the tunnel magnetoresistance of pseudo-spin-valve magnetic tunnel junction with a MgO tunnel barrier. *Applied Physics Letters* 90(212507):1-3.

Lin, M.T., C.H. Ho, Y.D. Yao, R.T. Huang, C.C. Liao, F.R. Chen and J.J. Kai. 2002. Interface characterization and thermal stability of Co/Al-O/CoFe spin-dependent tunnel junctions. *Journal of Applied Physics* 91(10):7475-7477.

Liu, L., H. Gong, Y. Wang, J. Wang, A.T.S. Wee and R. Liu. 2001. Annealing effects of Tantalum thin films sputtered on [001] Silicon substrate. *Materials Science Engineering* C (16):85-89.

Magnusson, J., E. Papadopoulou, P. Svedlindh and P. Nordblad. 1997. AC susceptibility of a paramagnetic Meissner effect sample. *Physica* C 297:317-325.

Meiklejohn, W. P. and C. P. Bean. 1957. New magnetic anisotropy. *Physical Review* B 105:904.

Miyazaki, T. and N. Tezuka. 1995. Giant magnetic tunneling effect in Fe/Al_2O_3/Fe Junction. *Journal of Magnetism and Magnetic Materials* 139(3):231.

Moodera, J.S., L.R. Kinder, T.M. Wong and R. Meservey. 1995. Large magnetoresistance at room temprature in ferromagnetic thin film tunnel junctions. *Physical review letters* 74(16):3273-3276.

Mott, N.F. 1936. The electrical conductivity of transition metals. *Proc. Roy. Soc. London* A 153:699.

Ng, V., J.F. Hu, A.O. Adeyeye, J.P. Wang and T.C. Chong. 2002. Radio frequency substrate bias effect on properties of Co thin film and multileyer structures. *Journal of Magnetism and Magnetic Materials* 247:339-344.

Park, M.H., Y.K. Honk, S.H. Gee, M.L. Mottern and T.W. Jang. 2002. Difference in coercivity between Co/Fe and Fe/Co bilayers. *Journal of Applied Physics* 91(10):7218-7220.

Parkin, S.S., C. Kaiser, A. Panchula, P.M. Rice, B. Hughes, M. Samant and S.H. Yang. 2004. Giant tunnelling magnetoresistance at room temperature with MgO (100) tunnel barriers. *Nature Materials* 3:862-867

Rottländer, P., M. Hehn, O. Lenoble and A. Schuhl. 2001. Tantalum oxide as an alternative low height tunnel barrier. *Applied Physics Letter* 78 (21): 3274-3276.

Schuhl, A. and Lacour, D. 2005. Spin dependent transport: GMR & TMR. *Comptes Rendus Physique*. Vol. 6, pp. 945-955.

Sharma, A., R. Brajpuriya, S. Tripathi and S.M. Chaudhari. 2005. Study of annealed Co thin films deposited by ion beam sputtering. *Journal of Vacuum Science Technology* A 24 (1):74-77.

Sharma, P. and A. Gupta. 2005. Effect of preparation condition on the soft magnetic properties of FeCuNbSiB thin film. *Journal of Magnetism and Magnetic Materials* 288:347-353.

Simmons, J.G. 1963. Generelized formula for the electric tunnel effect between similar electrodes seperated by a thin insulating film. *Journal of Applied Physics* 34(6):1793.

Sousa, R.C., J.J. Sun, V. Soares, P.P. Freitas, A. Kling, M.F. da Silva and J.C. Soares. 1998. *Applied Physics Letter* 73 (1998):3288.

Sun, J.J., V. Soares, P.P. Freitas, A. Kling, M.F. da Silva and J.C. Soares. 1998. Large tunneling magnetoresistance enhancement by thermal anneal. *Applied Physics Letters* 73:3288-3290.

Swerts, J., S. Vandelande, K. Temst and C.V. Haesendonck. 2004. Surface roughness effects on the magnetization reversal of polycrstalline Fe/Ag thin films. *Solid Stade Communications* 131:359-363.

Thomson, W. 1856. On the electro-dynamic qualities of metals: Effects of magnetization on the electric conductivity of Nickel and of Iron. *The Royal Society of London* 8:546-550.

Wang, D., C. Nordman, J.M. Daughton, Z. Qian and J. Fink. 2004. 70% TMR at room temperature for SDT sandwich junctions with CoFeB as free and reference layers. *IEEE Transaction on Magnetics* 40:2269-2271.

Wang, D., J.M. Daughton, D. Reed, W.D. Wang and J.Q. Wang. 2000. Magnetostatic coupling in spin dependent tunnel junctions. *IEEE Transactions on Magnetics*. 36(5):2802-2805

Yuasa, S., T. Nagahama, A. Fukushima, Y. Susuki and K. Ando. 2004. Giant room-temperature magnetoresistance in single-crystal Fe/MgO/Fe magnetic tunnel junctions. *Nature Materials* 3:868-871.